A Pilot Experiment on Infrasonic Lahar Detection at Mount Adams, Cascades: Ambient Infrasound and Wind-Noise Characterization at a Quiescent Stratovolcano

Richard W. Sanderson*1,2, Robin S. Matoza1,2, Rachel M. Haymon1, and Jamison H. Steidl2,

Abstract

Erosion, hydrothermal activity, and magmatism at volcanoes can cause large and unexpected mass wasting events. Large fluidized debris flows have occurred within the past 6000 yr at Mount Adams, Washington, and present a hazard to communities downstream. In August 2017, we began a pilot experiment to investigate the potential of infrasound arrays for detecting and tracking debris flows at Mount Adams. We deployed a telemetered four-element infrasound array (BEAR, 85 m aperture), ~11 km from a geologically unstable area where mass wasting has repeatedly originated. We present a preliminary analysis of BEAR data, representing a survey of the ambient infrasound and noise environment at this quiescent stratovolcano. Array processing reveals near continuous and persistent infrasound signals arriving from the direction of Mount Adams, which we hypothesize are fluvial sounds from the steep drainages on the southwest flank. We interpret observed fluctuations in the detectability of these signals as resulting from a combination of (1) wind-noise variations at the array, (2) changes in local infrasound propagation conditions associated with atmospheric boundary layer variability, and (3) changing water flow speeds and volumes in the channels due to freezing, thawing, and precipitation events. Suspected mass movement events during the study period are small (volumes $< 10^5 \text{ m}^3$ and durations < 2 min), with one of five visually confirmed events detected infrasonically at BEAR. We locate this small event, which satellite imagery suggests was a glacial avalanche, using three additional temporary arrays operating for five days in August 2018. Events large enough to threaten downstream communities would likely produce stronger infrasonic signals detectable at BEAR. In complement to recent literature demonstrating the potential for infrasonic detection of volcano mass movements (Allstadt et al., 2018), this study highlights the practical and computational challenges involved in identifying signals of interest in the expected noisy background environment of volcanic topography and drainages.

Cite this article as Sanderson, R. W., R. S. Matoza, R. M. Haymon, and J. H. Steidl (2021). A Pilot Experiment on Infrasonic Lahar Detection at Mount Adams, Cascades: Ambient Infrasound and Wind-Noise Characterization at a Quiescent Stratovolcano, Seismol. Res. Lett. XX, 1–22, doi: 10.1785/0220200361.

Supplemental Material

Introduction

Massive fluidized debris flows (lahars) originating from the upper slopes of volcanoes can occur without warning. Historically and recently, lahars have buried entire villages near volcanoes, with great loss of life (e.g., Pierson *et al.*, 1990; Major *et al.*, 2018). These potentially devastating, fastmoving flows pose an ongoing threat to people living in low-lying areas along drainages emanating from volcanoes. The study presented here is sited on Mount Adams in the Cascade Range of the Pacific Northwest, where large lahars have occurred within the past 6000 yr and are a significant

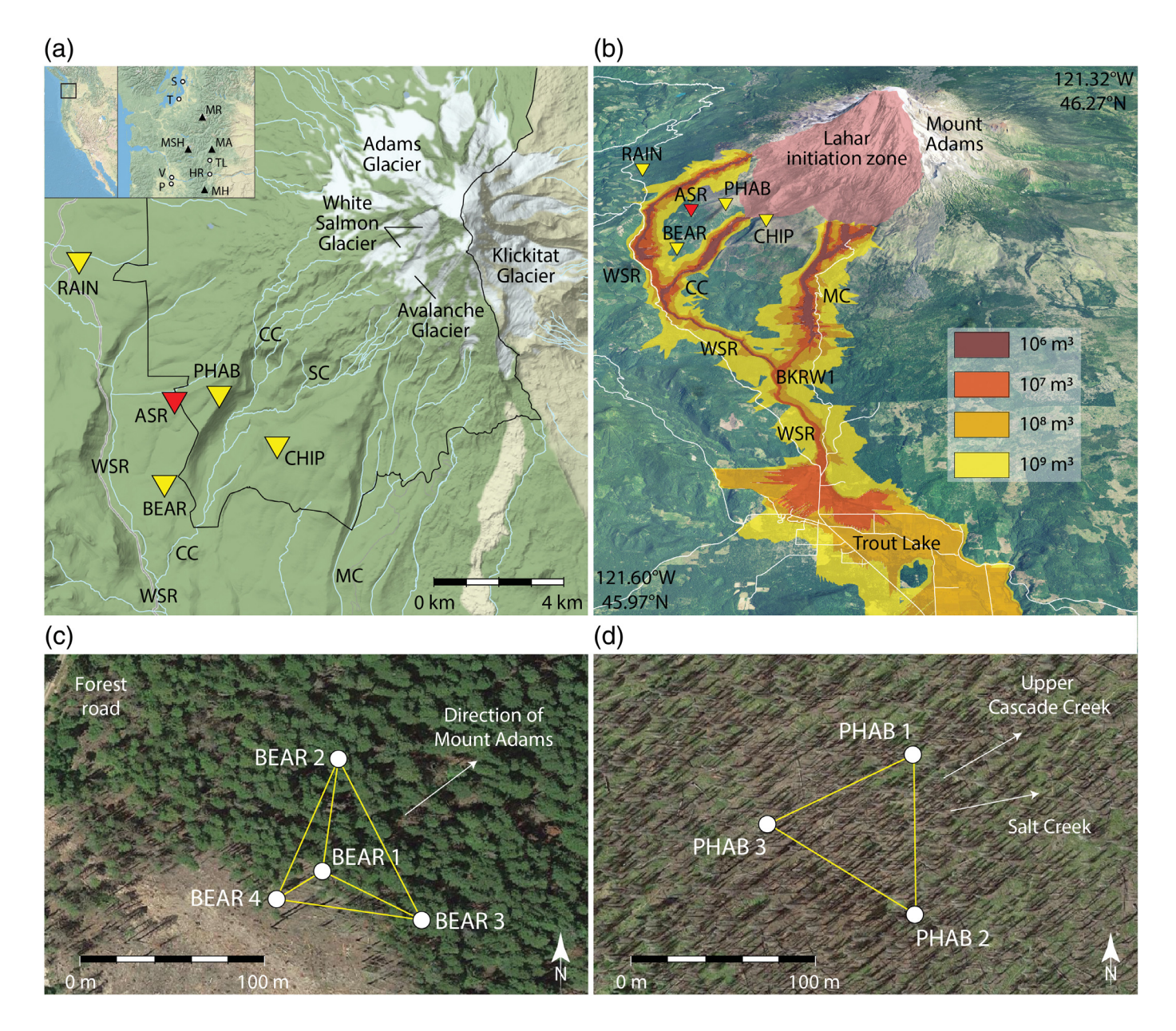
ongoing hazard to communities downstream (Griswold et al., 2018).

It is possible to detect the early stages of catastrophic lahars, and so potentially warn people to seek higher ground before the lahar arrives, but most endangered populations do not have

^{1.} Department of Earth Science, University of California, Santa Barbara, California, U.S.A., https://orcid.org/0000-0003-3772-4144 (RWS); https://orcid.org/0000-0003-4001-061X (RSM); https://orcid.org/0000-0003-4001-061X (RSM); https://orcid.org/0000-0003-0612-7654 (JHS)

^{*}Corresponding author: rws@ucsb.edu

[©] Seismological Society of America



lahar detection systems. Reviews of monitoring strategies for lahar and debris flows are provided by Arattano and Marchi (2008), Pierson *et al.* (2014), Stähli *et al.* (2015), Allstadt *et al.* (2018), and Hürlimann *et al.* (2019). Infrasound sensor arrays record acoustic waves propagating through the atmosphere at frequencies below the threshold of human hearing (<20 Hz) (Fee and Matoza, 2013; De Angelis *et al.*, 2019; Matoza *et al.*, 2019). Many kinds of surface mass movements at volcanoes (e.g., rockfalls, pyroclastic flows, and lahars) are known to produce distinctive infrasound signals (e.g., Allstadt *et al.*, 2018, and references therein).

To investigate the potential of infrasound for detecting and tracking lahars at Mount Adams, we conducted a pilot experiment. Since August 2017, we have operated a four-element telemetered infrasound array (SB.BEAR), located ~11 km from a hydrothermally weakened and unstable zone above the White Salmon and Avalanche Glaciers, where historical mass wasting

Figure 1. Important features in the Mount Adams study area. (a) The main panel gives an overview of the stations, glaciers, drainages, and wilderness boundary (black line). Insets are regional maps, showing nearby volcanoes and urban areas. (b) Modeled lahar inundation extents in the White Salmon River Valley (modified from Griswold et al., 2018). BKRW1 is a U.S. Forest Service weather station. (c) Geometry of the four subarrays at BEAR. (d) Geometry of PHAB, which has no subarrays. CC, Cascade Creek; HR, Hood River; MA, Mount Adams; MC, Morrison Creek; MH, Mount Hood; MR, Mount Rainier; MSH, Mount St. Helens; P, Portland; S, Seattle; SC, Salt Creek; T, Tacoma; TL, Trout Lake; V, Vancouver; WSR, White Salmon River.

has originated and future events are expected (Finn *et al.*, 2007; Fig. 1a,b). In August 2018, we temporarily deployed three additional three-element arrays (PHAB, CHIP, and RAIN), to help corroborate and locate signals recorded at BEAR. BEAR is scheduled for removal in mid-2021.

This article is organized as follows: first, we outline some of the relevant geological hazards at Mount Adams and the nature of the stations used in the study. Next, we describe our data-processing methods and the anticipated acoustic character of mass movement signals. Analysis of the ambient infrasound (e.g., Matoza *et al.*, 2013) and noise environment (e.g., Brown *et al.*, 2014) follows, including wind–noise impacts and arrivals likely of fluvial origin. This analysis focuses first on the long-term records from BEAR and then on insights contributed by the temporary infrasound arrays. We identify several event types in the data and isolate events that are candidates for mass movements. The timing, location, and character of a glacial avalanche is assessed in detail.

Study area

Mount Adams, one of the largest Cascade volcanoes, last erupted 540–2500 yr ago (Hildreth and Fierstein, 1995; Scott *et al.*, 1995) and has since continued to have active fumaroles near its summit (Hildreth and Fierstein, 1995; Vallance, 1999). Explosive eruptions that fragmented the core of the mountain, and hydrothermal activity that has altered the volcanic material to soft, low-strength hydrous minerals, together have produced 1.8 km³ of weak, unstable material in a bowl-shaped volume centered under the summit (Finn *et al.*, 2007). Water saturation within this rotten core volume increases potential for slope failure and generation of hazardous lahars (Finn *et al.*, 2007). Additional nonmagmatic forcing factors are snow loading, fracturing due to ice formation, pore pressure changes, erosion, and earthquakes (Vallance, 1999).

A large lahar, associated with eruptions \sim 6000 yr ago, flowed more than 40 km down the White Salmon River drainage (Vallance, 1999). At the current location of Trout Lake, Washington, 27 km south of Mount Adams, the lahar left deposits up to 20 m thick and spread out to form the present floor of the Trout Lake Valley. Figure 1b gives an indication of the path of the 6.6×10^7 m³ flow. Another smaller lahar, \sim 250 yr ago, reached the location of the town and formed a deposit up to 4 m thick (Vallance, 1999; Griswold *et al.*, 2018). There is currently no evidence to suggest that this recent lahar was triggered by an eruption or unrest.

Continued instability of the Mount Adams summit region is demonstrated by recurring debris flows and lahars, with lengths of up to 3 km on subdecadal timescales (Norris, 1994; Scott, 2010; Allstadt *et al.*, 2017; Lloyd, 2018) and up to 8 km during the past 100 yr (Vallance, 1999). Ultimately, it would be desirable to detect these small-to-moderate-sized events, because larger slope failures are expected to initiate similarly.

Methodology

The equipment, data processing, and anticipated event characteristics for this study are described in the following. Infrasound arrays typically consist of at least three microbarometer pressure-sensing elements arranged spatially on the

ground with an aperture of about 50–100 m, connected to a single digitizer and telemetry system (e.g., Garcés *et al.*, 2003; Matoza *et al.*, 2007). Siting arrays close to volcanoes with direct line of sight to the upper slopes facilitates rapid detection and localization of acoustic signals from surface events, but this must be balanced with other logistics, including site-noise conditions (e.g., Matoza *et al.*, 2007).

Mass wasting infrasound may be identified based on multiple signal features, but this is still an active area of research (Allstadt et al., 2018). Array processing helps significantly by providing direction-of-arrival information from one or more arrays, with changes in back azimuth and inclination angle (a measure of altitude) over time indicating a moving source (Ulivieri et al., 2011; Johnson and Palma, 2015; Marchetti et al., 2015; Thüring et al., 2015; Bosa et al., 2020). Array processing is also critical in identifying these coherent infrasonic signals within incoherent wind noise, because wind-noise waveforms can superficially resemble mass movement signals (Matoza et al., 2019). Similar methods have been investigated for mass movement events in nonvolcanic settings (e.g., Adam et al., 1998; Yount et al., 2008; Leng et al., 2017; Moore et al., 2017; Johnson et al., 2019; Marchetti et al., 2019). We build on these studies to investigate the potential for real-time lahar detection at Mount Adams, considering realistic ambient infrasound and noise conditions near the drainages of this quiescent stratovolcano.

BEAR array

BEAR is our long-term infrasound array at Mount Adams. Siting an array close to the primary drainages from the unstable southwest flank presumably enhances the potential for mass movement detection. The Gifford Pinchot National Forest covers the broader region, however, with much of Mount Adams itself designated a wilderness zone (Fig. 1a). Long-term installations inside the wilderness boundary are heavily restricted; consequently, site locations close to likely source zones on the upper slopes are limited. The resulting design and location of the BEAR array still allows for real-time data acquisition, and minimization of permit issues.

Four Hyperion IFS-3111 infrasound sensors comprise the BEAR array, which has an aperture of 85 m (Fig. 1c). Each sensor has a high-frequency shroud for wind-noise reduction. These sensors provide a frequency response within 3 dB from 0.01 to 100 Hz, low self-noise floor (≤0.1 mPa), and high-dynamic range (120 dB). Valve boxes cover the sensors to provide basic protection from animals and snow accumulation. Wind-noise attenuation domes (e.g., Raspet *et al.*, 2019) were not deployed due to the potential for crushing by the winter snowpack. A technical issue led to limited sensor sensitivity through 28 September 2017, after which performance was nominal. All dates and times provided are in Coordinated Universal Time (UTC). Further information on station siting and design is provided in the supplemental material available to this article.

Temporary infrasound arrays

The temporary infrasound arrays at PHAB (Fig. 1d), CHIP, and RAIN were deployed between 26 and 31 August 2018, to provide azimuthal coverage of anticipated signal sources on the southwest side of Mount Adams as well as other noise sources in the area. Data from these temporary arrays were recorded locally with no telemetry link. Respective array apertures are ~80, ~75, and ~70 m. PHAB and CHIP were located on ridgetops on either side of the main drainage within the Mount Adams Wilderness (Fig. 1), with RAIN located at a lower altitude, and in denser forest to the west of Mount Adams.

At each temporary array, the Chaparral Model 60-UHP infrasound sensors sit within foam wind filters, but are otherwise exposed to the atmosphere. Sensor performance specifications are comparable to those at BEAR, except for the greater selfnoise floor here (~25 mPa), and lower-dynamic range (109 dB).

Seismic data

To detect seismicity at Mount Adams, the Pacific Northwest Seismic Network (PNSN) maintains a single-component shortperiod seismic station UW.ASR on Stagman Ridge (Moran, 2005), 2.5 km from our infrasound array (Fig. 1a,b). Because debris-laden rivers are also strong generators of seismicity (e.g., Hsu et al., 2011; Tsai et al., 2012; Roth et al., 2016; Walsh et al., 2020), seismic data can help corroborate ambiguous infrasound signals or otherwise clarify when our stations are not detecting known events. Unfortunately, station ASR had impaired sensitivity for ~75% of 2017-2019 (Natalie Chow, Designer and Program Coordinator, PNSN, written comm., 2020). Many time intervals contain only electronic noise or have the sensor response focused between 10 and 30 Hz. Observations of five seismogenic mass movement events at Mount Adams between 1983 and 2012 are presented by Norris (1994) and Allstadt et al. (2017). These events were recorded on regional stations to distances of 183 km.

Data processing

The array processing scheme is described in the following, as are expected event characteristics. We use the progressive multi-channel correlation (PMCC) array processing algorithm (Cansi, 1995; Le Pichon *et al.*, 2010; Matoza *et al.*, 2013) as a first step to analyze the infrasound waveform data. PMCC estimates parameters of coherent plane waves at the array, including back azimuth, apparent velocity, signal frequency, and F-statistic (akin to the signal-to-noise ratio [SNR]). The PMCC maximum amplitude estimates are approximately equal to the peak-to-peak amplitude values of the corresponding time series. Apparent velocity ($v_{\rm app}$) values from PMCC can be used to infer wavefront incidence angles above the horizontal, $\theta_H = \cos^{-1}(v_{\rm int}/v_{\rm app})$, by assuming an intrinsic adiabatic velocity, $v_{\rm int} \approx \sqrt{(403 \cdot T)}$. T is the temperature in Kelvin.

PMCC searches in time-frequency space for plane-wave arrivals consistent across multiple subarrays with similar

wavefront properties. This approach helps reduce uncertainty in cases of spatial aliasing (Cansi and Le Pichon, 2009; Marty, 2019). The four-element BEAR array has four possible subarrays (three-sensor triads that are subsets of the full array) (Fig. 1c). An array bandwidth of ~0.3–8 Hz balances wavefield estimation accuracy and spatial aliasing ambiguity (Garcés, 2013). Higher-frequency events may be well resolved if signals are clear, short, and broadband (Garcés, 2013; de Groot-Hedlin et al., 2014). We include data up to 50 Hz in this study (i.e., low audio), a range that is important for identifying small acoustic sources. For simplicity here, the term infrasound is used to include this extended frequency band.

Wavefront similarity is indicated by a low consistency value, that is, the sum of the time delays between array elements. A successful search will result in a record of the wavefield parameters for that time window and frequency-band combination—termed a pixel. Related pixels are then grouped into families, with higher pixel counts indicating more robust results. PMCC is an efficient array processing method, making it suitable for real-time applications. One day of typical BEAR data (100 samples per second) requires ~2.5 hr to process on a 3.1 GHz processor. We provide processing parameters for PMCC in the supplemental material.

Signal characteristics. To identify potential events at Mount Adams, we look for transient signals in the raw waveform data, together with coherent array processing results that arrive from an appropriate azimuth range with an acoustic velocity. We also examine signal amplitude, robustness of the detection family, and changes in back azimuth indicative of moving sources. Anticipated lahar signal properties include emergent, broadband seismoacoustic waveforms, which last from tens of minutes to hours in duration. For lahars capable of reaching up to 20 km, amplitudes of 2.5 Pa may be expected at a distance of 4 km during the peak of the event (equivalent to 10 Pa at 1 km), although, this is a value based on limited observations (Johnson and Palma, 2015). Waveform durations from the collapse, fall, and flow of consolidated or unconsolidated material would likely be from tens of seconds to several minutes (Allstadt et al., 2018, and references therein). Onsets could be emergent or impulsive according to the mode of initiation, with most energy concentrated from 1 to 10 Hz, depending on volume and composition. Amplitudes for such events can vary considerably, with reduced pressure observations of 1 Pa at 1 km for small rockfalls and ice avalanches (e.g., Havens et al., 2014; Johnson and Ronan, 2015), to 110 Pa at 1 km for very large avalanches (Allstadt et al., 2017). Machinelearning-based classification and location schemes are increasingly being applied to mass wasting monitoring applications (e.g., Allstadt et al., 2018, and references therein; Ye et al., 2019; Liu et al., 2020; Wenner et al., 2020).

When analyzing waveforms alongside PMCC results, denoising steps help to isolate signals of interest. Here, we apply

two denoising tools on a case-by-case basis to time-delayed beams during postprocessing. First, BCseis (Langston and Mousavi, 2018), which uses an adaptive block thresholding approach in the frequency domain, and (2) an iterative Wiener filter (Plapous *et al.*, 2006), which minimizes the difference between noise-contaminated signals and a designated noise-only section to isolate the signals of interest.

Results

Our results include characteristics of background infrasound from the long-term BEAR infrasound array, and records of mass wasting and other activity. Data from both the temporary infrasound arrays and BEAR are used to isolate some of the sources of the coherent background arrivals and to locate and model a glacial avalanche.

BEAR array

Background signals. Array processing results from BEAR reveal near-continuous and persistent infrasound signals arriving from the direction of Mount Adams (back azimuths 30°-65°; Fig. 2a), which we hypothesize result from turbulent fluvial processes, such as rapids and waterfalls (e.g., Johnson et al., 2006; Huang et al., 2008; Schmandt et al., 2013; Feng et al., 2014; Ronan et al., 2017; Anderson et al., 2019) in the steeper upper portions of the Cascade Creek and Salt Creek drainages. Observed fluctuations in the detectability of these signals over time likely result from a combination of: (1) variation in wind-noise levels at the array (e.g., Woodward et al., 2005; Matoza et al., 2011), (2) changes in local infrasound propagation conditions associated with atmospheric boundary layer variability (e.g., Fee and Garcés, 2007; Matoza et al., 2009; Wilson et al., 2015; Kim et al., 2018), and (3) changing flow speeds in the channels (assuming the infrasound is fluvial in origin). By covering the infrasound sensors, higher snowpacks are expected to reduce wind noise, as well as increase the attenuation of signals of interest, particularly, at higher frequencies (Adam et al., 1998). The number of detections from the 30° to 65° azimuth range is the highest during the summer (May-August; Fig. 2b,c), consistent with an increase in glacial meltwater flow. Winter (November-February) detections for this direction may relate to increased flow from rainfall and rain-on-snow melting during storms (Fig. 2d,e). Corresponding mean signal frequencies are typically 3-20 Hz throughout the year—a similar range to whitewater features described by Anderson et al. (2019). In the 30°-65° azimuth range, apparent velocities are 330-360 m/s, indicating low incident angles and local signal sources. The time periods designated as summer and winter are derived from Figure 2a, being equal length and equally spaced periods that exhibit distinct characteristics.

The BEAR array also records seasonally dependent 3–20 Hz signals in almost all directions disjoint from Mount Adams (Fig. 2). It is likely that this wide distribution of detections is also

tied to high-gradient streams and waterfalls, which cover the region. An initial analysis (presented in the supplemental material) shows similar temporal trends for PMCC detection quantities and regional river discharge. The story is complex, given the variable input of rainfall and snow melt in the disparate watersheds, as well as fluctuating atmospheric conditions. In addition, waterfalls each have their own seismoacoustic signature based on height, plunge style, topographic directivity, and flow volume (Burtin et al., 2008; Díaz et al., 2014; Anderson et al., 2019). Future work with more weather and hydrological sensors than are currently deployed near the field site would help untangle the factors directing this fluvial infrasound.

The most dominant feature of the PMCC processing results is the coherent background infrasound from the Pacific Ocean (microbaroms) during the winter. Wave–wave interaction primarily generates such signals, typically resulting in a peak between 0.1 and 0.5 Hz (Bowman et al., 2005). Wave–shore interaction may contribute frequencies up to 20 Hz (Garcés et al., 2006), although, significant attenuation would be expected at this distance. During the summer, microbarom signals are infrequently observed (Fig. 2c) due to the change in dominant stratospheric wind direction from eastward blowing to westward blowing (Le Pichon et al., 2009), as well as a decrease in storm activity.

Another dominant feature in the PMCC results is persistent year-round higher-frequency signal content in the low-audio range (20–50 Hz), likely of anthropogenic origin from passing aircraft and surrounding urban areas (Matoza *et al.*, 2007; Campus and Christie, 2010, and references therein; Pilger *et al.*, 2018). The corresponding source directions are predominantly from south to southwest (a range covering Hood River, Portland, and Vancouver) (Fig. 1a).

Figure 3 shows probabilistic power spectral density (PSD) plots (McNamara and Buland, 2004) for the time periods covered by Figure 2. The principal differences between the summer and winter periods are in the 0.1–10 Hz band, with a much wider range in noise level during the summer and a prominent microbarom peak in the winter. These spectra span the full range of global noise models (Bowman *et al.*, 2007; Brown *et al.*, 2014).

Mass wasting and other activity. Having characterized the background infrasound at BEAR, we next examine records from BEAR (and ASR), at times of reported or imaged mass movements at Mount Adams. We then filter the PMCC results to isolate additional mass wasting candidates and other event types.

Search for signals associated with witnessed small events. Table 1 lists notable events at Mount Adams between June 2017 and August 2020, as witnessed by local observers or identified in available satellite imagery. Satellite images are four-band PlanetScope Scenes (3 m resolution, see Data and

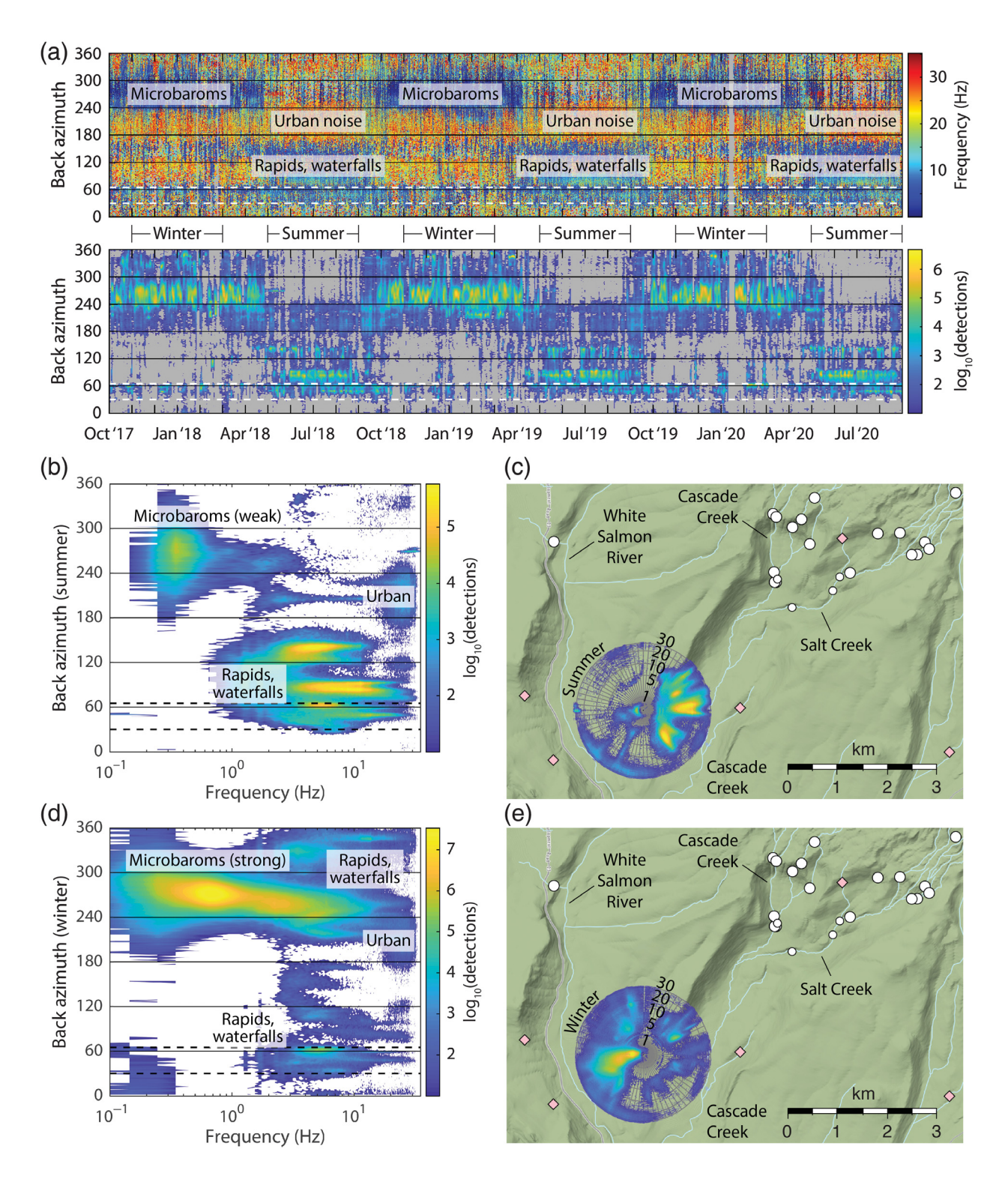
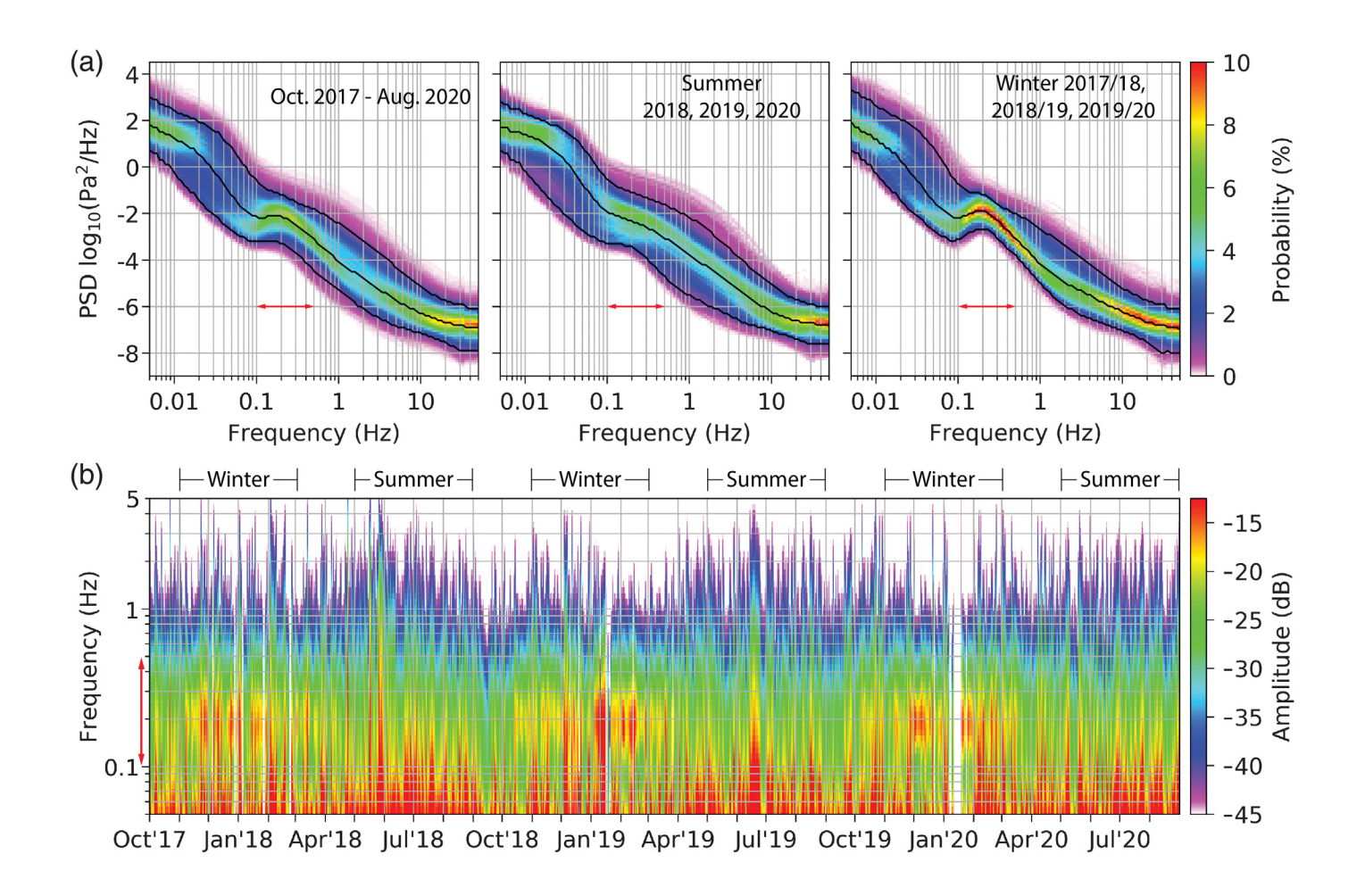


Figure 2. Seasonal trends in infrasound detections, illustrating distinct source types and locations. (a) Progressive multi-channel correlation (PMCC) results at BEAR, plotted as back azimuth versus time. The top panel is color coded by family mean frequency, and the bottom panel is color coded by the log number of detections in the top panel. Bin sizes are one day in time and 0.1 Hz in frequency. Gray indicates <10 detections. White-dashed lines bracket the back-azimuth range to the upper Cascade Creek and Salt Creek basins (colored black in panels b,d).

(b) 2D histogram of summer detections (May–August). Bin sizes are 1.0° in azimuth and 0.1 Hz in frequency. Absence of color indicates <10 detections. (c) Polar 2D histogram for summer detections, with higher frequencies at increasing radius. The positions of waterfalls 5–10 m and >10 m in total height are marked with small and large circles, with selected high-gradient streams as diamonds. Panels (d,e) are the same as panels (b,c), but for winter detections (November–February).



Resources), which were visually inspected only during time frames indicated to be of interest by local witness reports or seismoacoustic data. The table includes debris flows, glacial movements, and changes in river character, which may indicate potential upstream debris flows in the preceding hours. Since the installation of BEAR, there have been five visually confirmed mass movements: two in 2017 and one each in 2018, 2019, and 2020. This number is likely an underestimate. In cold months in particular, the mountain often is hidden by clouds, and human access is limited, making visual observations of events difficult. All observed events took place from June to September, when temperatures are relatively warm, snow is melting, and the greatest potential for instability occurs (e.g., Mills, 1991). The 28 August 2018 event is the only entry from Table 1 for which we could find clearly attributable seismoacoustic signals. The main complications are: (1) relatively small amplitude events; (2) poor knowledge of the timing of the events; (3) coherent array detections (clutter) regularly coming from the expected azimuths; (4) waveform characteristics are likely weak and emergent, and superficially similar to wind noise; (5) unknown local propagation conditions; and (6) limited numbers of stations and data types. In conclusion, few obvious waveforms correspond to the events of Table 1, because these events likely are at or below station detection thresholds.

Figure 3. Seasonal trends in ambient infrasound, reflecting stronger microbaroms in winter and higher wind noise in summer. (a) Probabilistic power spectral density (PSD) estimates of BEAR (channel 1) infrasound data for (1) the whole study period, (2) summers, and (3) winters. These time periods correspond to those in Figure 2. All parameters follow those by McNamara and Buland (2004). Time windows used to estimate the PSDs are 1 hr long with 50% overlap and a 10% cosine taper. The color scheme indicates the percentage of counts in each amplitude—frequency bin out of the total count at that frequency. Bins are 1 dB by 1/8 of an octave, with powers averaged over a full octave. Black lines are the 5th, 50th, and 95th percentiles for the data in each plot. Red arrows indicate the range of the microbarom peak (0.1–0.5 Hz). (b) The temporal evolution of the PSD for the whole study period.

To illustrate the previous issues, Figure 4 shows selected processing results for the speculated time period of the July 2018 debris flow event. Data types include PMCC processing results (back azimuth, cross-correlation, maximum amplitude, each color coded by family mean frequency), filtered beamformed data, and spectral content over time. Diurnal winds are expected to present with power inversely proportional to frequency, but, notably here, the relative power in each band is inconsistent over time. The wind bursts interrupt the

Witnessed Accounts of Physical Processes at Mount Adams from 2017 to 2020, Which May Have Produced Seismoacoustic Signals, and Brief Notes on Any Corresponding Geophysical Data TABLE 1

Date and Time (yyyy/mm/dd hh:mm:ss)	Location	Description	Infrasound (BEAR)	Seismic (ASR)	Time Constraints
2017/06/03 18:12:07–2017/ 06/04 18:12:40	Battlement Ridge to Klickitat Glacier, southeast Mount Adams	Debris flow ~1.6 km long, $400,000 \text{ m}^3$ (Darryl Lloyd, written comm., 2017)	Not installed	Most likely candidate a broadband envelope on 3 June at 21:01, duration 5 min	Satellite images on 3 (not seen) and 4 June (seen). In-person observation on 6 June (Darryl Lloyd, written comm., 2017)
~2017/09/05~2017/09/11	Below summit onto White Salmon and Avalanche Glaciers	Debris flow from ~3350 to 2750 m elevation	Not fully operating and no clear signals	Frequent emergent and impulsive events. Sustained signal on 4 September at 13:00–22:00	White Salmon River muddy on 6 September. In-person view on 11 September. Undear in satellite images
2017/09/15 19:30–20:00	Above Horseshoe Meadows, southwest Mount Adams	"Rockslide" sounds	Not fully operating and no clear signals	Elevated seismic signals from 19:35 to 20:35	Noises reported by hikers
~2018/07/10-2018/07/11	White Salmon River in Trout Lake	Muddy flow	No strong candidate signals. Persistent noise	Sustained noise. Several prominent In-person observation on 11 July. impulsive events	In-person observation on 11 July. Satellite images show minor snow melt
2018/07/20–2018/07/27, possibly earlier, or as late as 2018/08/05	White Salmon Glacier headwall onto Avalanche Glacier	Small debris flow from ~3600 to 2700 m elevation, 1.4 km distance (Darryl Lloyd, written comm., 2018)	Strong diurnal wind noise. Few robust candidate signals. Broadband impulsive signals from ~22:00 4 August to ~03:00 5 August during an intense storm are primarily consistent with thunder. Some back azimuths during the storm coincide with nearby sources of water turbulence	Frequent impulsive events amidst diurnal noise. Candidate signals on 21 July at 16:37 and 27 July at 14:36. Clear broadband signals during storm 4 August at ~22:00 to 5 August at ~03:00	In-person observations on 20 July (potentially not seen), 27 July (potentially seen), and 5 August (seen). Unclear in satellite images
~2018/07/28–2018/07/30	White Salmon River in Trout Lake	Muddy flow	Few clear events with no strong candidate signals, noisy background	Long noisy periods (only some diurnal), frequent events, no standout candidates	In-person observation on 29 and 30 July. Satellite images show some snow melt
2018/08/08–2018/08/09	White Salmon Glacier	Noises heard	Prominent event on 9 August at 20:22, but PMCC metrics inconsistent with a local origin. Otherwise few clear events	Frequent impulsive events, more commonly during daytime when hot. Includes remote event on 9 August at 20:22	Noises reported by hikers. Satellite images show widening crevasses on the upper White Salmon Glacier on 8–10 August
2018/08/24 21:34:54–2018/ 08/28 18:29:25	White Salmon Glacier	Glacial avalanche (not witnessed in person)	Clear impulsive broadband arrivals on all four infrasound arrays on 28 August at ~16:01	~16:01 28 August 2018 event is just above background seismically	Satellite images on 24 (not seen) and 28 August (seen)

The "Date and Time" column gives a window during which the event may have occurred (or did), given the observations in the "Time Constraints" column. All times are UTC. Seismometer response was impaired <10 Hz during events from 2017 to 2018, and impaired at all frequencies for the 2019 event. PMCC, progressive multi-channel correlation. (Continued next page.)

Witnessed Accounts of Physical Processes at Mount Adams from 2017 to 2020, Which May Have Produced Seismoacoustic Signals, and Brief Notes on Any Corresponding Geophysical Data TABLE 1 (continued)

Date and Time (yyyy/mm/dd hh:mm:ss) Location	Location	Description	Infrasound (BEAR)	Seismic (ASR)	Time Constraints
2018/08/28 22:48–23:08	White Salmon Glacier	Noises heard	Strong background noise, no clear Impulsive signals at 22:37–22:45 waveforms, but several viable (earlier than observations) PMCC detections	Impulsive signals at 22:37–22:45 (earlier than observations)	In-person observation. Satellite images show no significant glacier changes
2019/06/08–2019/06/15	Below summit onto Avalanche Glacier	Debris flow from ~3400 to 2800 m elevation, 900 m distance	Strong diurnal wind noise. PMCC shows two potential detections on 12 June at ~03:28, but metrics are not robust	Potentially a series of four pulses on 11 June at 17:49, duration 1.5 min	Strong diurnal wind noise. PMCC Potentially a series of four pulses on In-person view on 8 June (not seen) and shows two potential detections on 11 June at 17:49, duration 1.5 min 15 June (seen). Satellite images on 11 12 June at ~03:28, but metrics are not robust
~2020/07/04 22:30	Above Stagman Ridge, southwest Mount Adams	"Avalanche" sounds	No distinct waveforms or potential No distinct waveforms PMCC detections	No distinct waveforms	Noises reported by hikers. Unclear in satellite images
~2020/08/31 01:45, possibly extends before and after by several hours	Above tree line on southwest Mount Adams, toward Williams Mine	Rockslide	No distinct waveforms or potential Few distinct waveforms during PMCC detections during ±2 hr. Large impulsive glitch-lik signal at 01:08	Few distinct waveforms during ±2 hr. Large impulsive glitch-like signal at 01:08	In-person view during event. Undear in satellite images

The "Date and Time" column gives a window during which the event may have occurred (or did), given the observations in the "Time Constraints" column. All times are UTC. Seismometer response was impaired <10 Hz during events from 2017 to 2018, and impaired at all frequencies for the 2019 event. PMCC, progressive multi-channel correlation.

higher-frequency background PMCC detections in Figure 4 (with similar observations by Matoza *et al.*, 2009; Green *et al.*, 2012; the time series in Figs. 2 and 3 also show a similar relation between PMCC detection gaps and wind bursts). Lower-frequency detections are more continuous, particularly, on 20 and 21 July. The next section shows that there are no clear detection candidates for the July 2018 debris flow when considering appropriate PMCC wave parameter combinations.

Distilling and classifying automatically detected signals. Following our search for signals associated with known mass movements, we now aim to identify instances of such events on the upper slopes of Mount Adams for which we do not have first-hand accounts. We isolate possibly associated PMCC detections by requiring positive SNRs (F-statistic ≥1.5, peakto-peak amplitude ≥0.1 Pa), appropriate locations (back azimuth 40°-55°, apparent velocity 330-360 m/s), with reasonable thresholds (number of pixels \geq 35, cross-correlation \geq 0.6). We also limit results to those with mean frequency ≥5 Hz to avoid some fluvial detections. Since August 2017, there have been 36 events matching these criteria. PMCC processing results for these events are included in the supplemental material. Such events do not, however, coincide with those in Table 1, other than that on 28 August 2018. This remains the case with no minimum amplitude (which gives 444 detections).

Using the presumed waveform characteristics (the Data Processing section; Allstadt et al., 2018) as well as weather data (from Ventusky, see Data and Resources), we classify 12 of the 36 events as mass wasting candidates. Durations range from 20 to 90 s, with amplitudes up to ~0.22 Pa. In the example in Figure 5a, ASR first registers the direct seismic arrival at 7 s and then an acoustic component as a ground-coupled airwave (GCA) at 37 s. BEAR records the direct airwave ~5.4 s later. The acoustic arrival times and PMCC back azimuth (44.3°) indicate a source region at ~2000 m elevation (assuming a velocity of 333 m/s, appropriate for a mean path temperature of 2 °C). The corresponding origin time would be ~14 s and may relate to the broadband seismic component. Eleven of the twelve mass movement candidates have similar back azimuths (42°-46°), spanning the White Salmon Glacier. The remaining event aligns with the Avalanche Glacier headwall (46°-49°), from which multiple debris fans indicate minor ongoing rockfall. In the next section, we more fully analyze the 28 August 2018 event, which was detected by the three temporary infrasound arrays, in addition to BEAR, and is the only one of these mass movement candidate events to clearly appear in satellite imagery.

We interpret 18 of the 36 events as thunder (e.g., Farges and Blanc, 2010), occurring as part of sequences. Each instance typically has an erratic waveform 10–30 s in duration with an amplitude <1 Pa (Fig. 5c), although, events of up to 4 Pa and >60 s have been recorded. Spectra tend to be even and broadband, though some spectra peak <10 Hz, perhaps

indicating relatively distant sources (Bass, 1980; Assink et al., 2008). When ASR is operational, thunder is typically registered via weak GCAs, with arrival times relative to BEAR dictated by the back azimuth. The absence of direct seismic arrivals for these events reduces the probability of these events being mass movements. Few of the hundreds of these thunder signals remain after parsing the PMCC detections; thus, our simple PMCC bulletin selection criteria are useful for an initial basic data screening. A more robust set of discriminators may be required, however, because the character of thunder can vary widely (e.g., Johnson et al., 2011; Liu et al., 2015; Marchetti et al., 2019; Haney et al., 2020), and repeated surges of fluidized debris flows may produce similar sets of signals (e.g., Kogelnig et al., 2014; Liu et al., 2015).

The remaining six events are impulsive with short codas, lasting 0.5-3 s, and spanning 3-30+ Hz in frequency. Four of the examples have negative first motions (Fig. 5d). These events may be icequakes (comparable to those described by Lombardi *et al.*, 2019, with Richardson *et al.*, 2012, and Allstadt and Malone, 2014, being other useful references) or possibly large tree-fall events. We rule out electromagnetic interference, given the acoustic travel times, general absence of thunderstorms, and similar amplitudes on each sensor (vs. Haney *et al.*, 2020). Gun shots are also unlikely, as such signals are typically $\ll 0.5$ s in duration (e.g., Maher and Shaw, 2008).

PHAB, CHIP, and RAIN arrays

As with the BEAR results earlier, we first address the origins of the background signals recorded by these temporary arrays and then proceed to an example of mass wasting. These results help illustrate the challenges relating to site selection and source characterization.

Background signals. PMCC detection results for each station are presented in Figure 6, with a focus on identifying any arrivals from the waterfalls located in the upper Cascade Creek and Salt Creek basins (Figs. 1 and 2). We retain detections >2 Hz to limit inclusion of microbaroms. Of the temporary stations, CHIP has the most detections within the back-azimuth band, with PHAB not indicating any sustained signal sources. At RAIN, some sustained detections occur, though in a back-azimuth range of 82–96°, corresponding to the sources either nearby RAIN, or higher up Mount Adams, in the region of the White Salmon and Avalanche Glaciers.

To constrain source locations, we apply an automated cross-bearings approach with the IMS-vASC algorithm (Matoza et al., 2017). IMS-vASC uses a grid search to tally the number of intersecting back azimuths over time. Here, we use a grid resolution of 0.005°. Figure 7 shows sample results, highlighting intersections of ≥20 pixels between the nearest station and at least one other station. Other requirements are family frequency ranges of 2–35 Hz and an azimuth deviation allowance of 2°, to limit results to the principal local sources within ~20 km. Figure 7

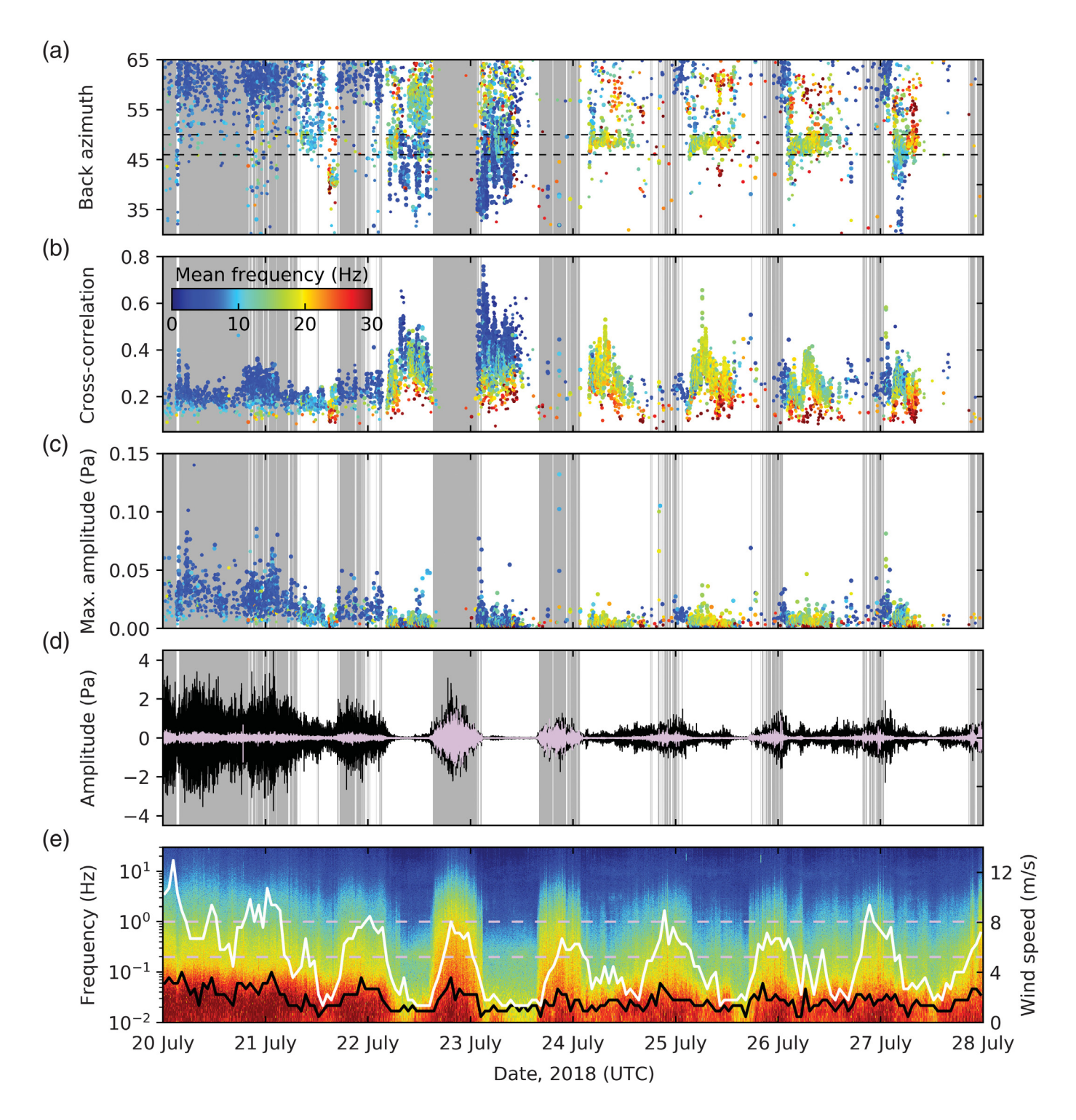


Figure 4. BEAR infrasound analysis for period spanning speculated occurrence of a debris flow at Mount Adams (as per eye witness details in Table 1), showing how wind noise can affect event detectability. (a–c) PMCC results limited to those detections with back azimuths from 30°–65°, which covers the majority of Mount Adams. Horizontal dashed lines cover the expected event back-azimuth range. Detections are color coded by family mean frequency. Incoherent wind noise from 0.2 to 1.0 Hz correlates well with gaps in high-frequency PMCC detections, with background shading applied if the PSD sum from 0.2 to 1.0 Hz exceeds 0.6 Pa²/Hz (5.5 min bins).

(d) Beamformed infrasound for a back azimuth of 48° and apparent velocity of 350 m/s, values appropriate to sources traversing the Avalanche Glacier. Waveforms are filtered before beamforming as follows: 0.01–0.2 Hz (black trace) and 0.2–1.0 Hz (purple trace). (e) A spectrogram of unfiltered beamformed infrasound, with dashed lines at 0.2 and 1.0 Hz. PSD is plotted on a log scale. Mean wind speed (solid black line) and maximum wind speed (solid white line) are from the U.S. Forest Service station at BKRW1 (Fig. 1b). Characteristics of signals from debris flows are either absent (no events occurred) or cannot be easily identified with such analysis.

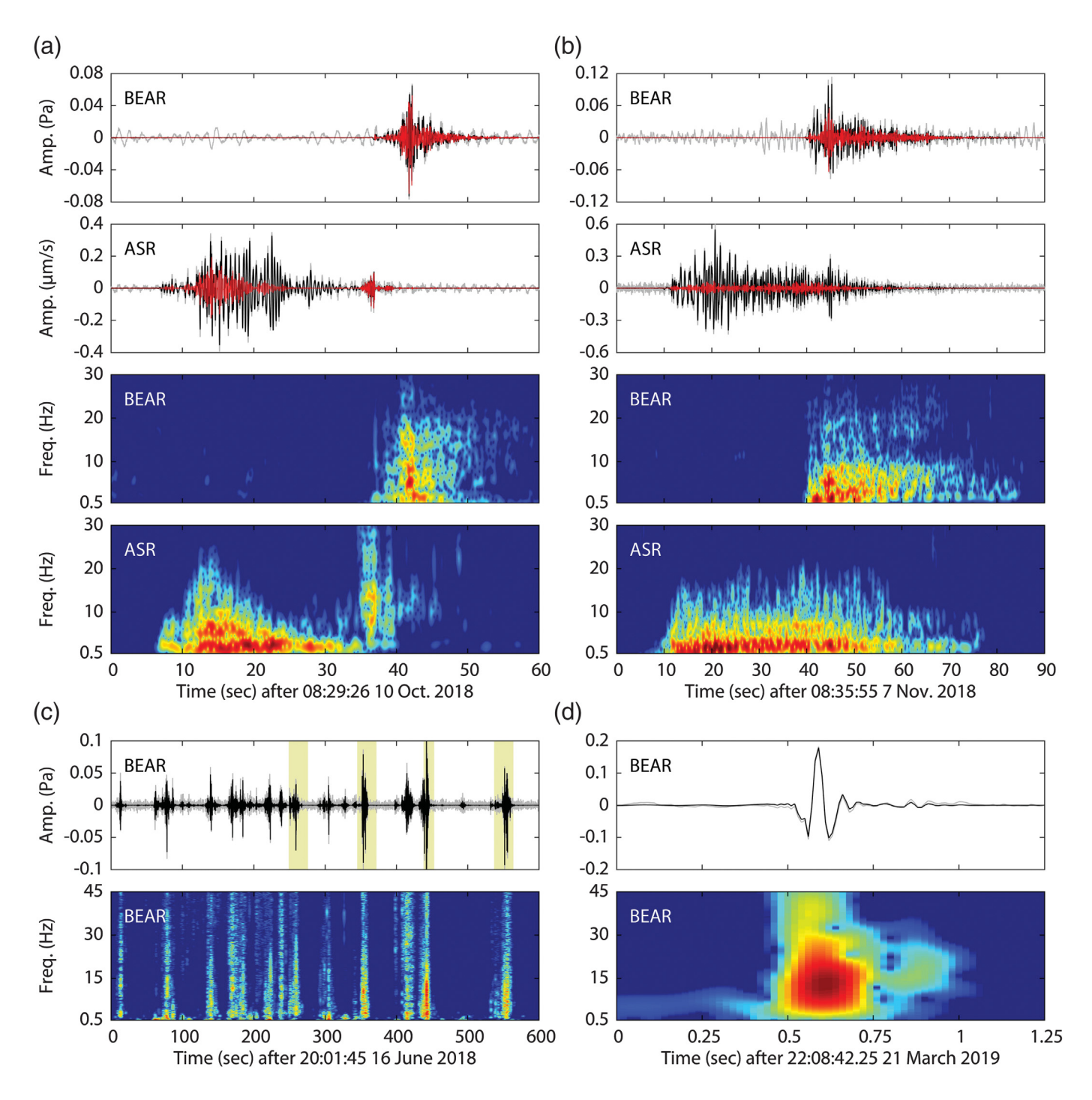


Figure 5. Examples of several event types that have back azimuths coincident with Mount Adams. (a) Potential mass wasting event from 10 October 2018 recorded at BEAR and ASR. A ground-coupled airwave (GCA) arrives at ASR at ~37 s. (b) A potential mass wasting event from 7 November 2018. Any GCAs at ASR are unclear in this case. (c) Thunder events at BEAR. Yellow-highlighted signals are those that coincidentally met the PMCC event parsing criteria. (d) Impulsive event example from 21 March

2019, possibly caused by an icequake or tree fall. In all figure parts, gray traces are >0.5 Hz, black traces are denoised using BCseis, and red traces are black traces >4 Hz. Infrasound traces have been beamformed using back azimuth and apparent velocity values from PMCC. The spectrogram plots PSD on a log scale, with warm colors indicating relatively high values and cold colors indicating relatively low values.

also shows the location of waterfalls as well as selected high-gradient streams, each of which may be potential signal sources. Waterfall data are primarily via the Northwest Waterfall

Survey (see Data and Resources). We find a general coincidence between these fluvial features and the back azimuths where topography and propagation conditions allow. Line of sight is

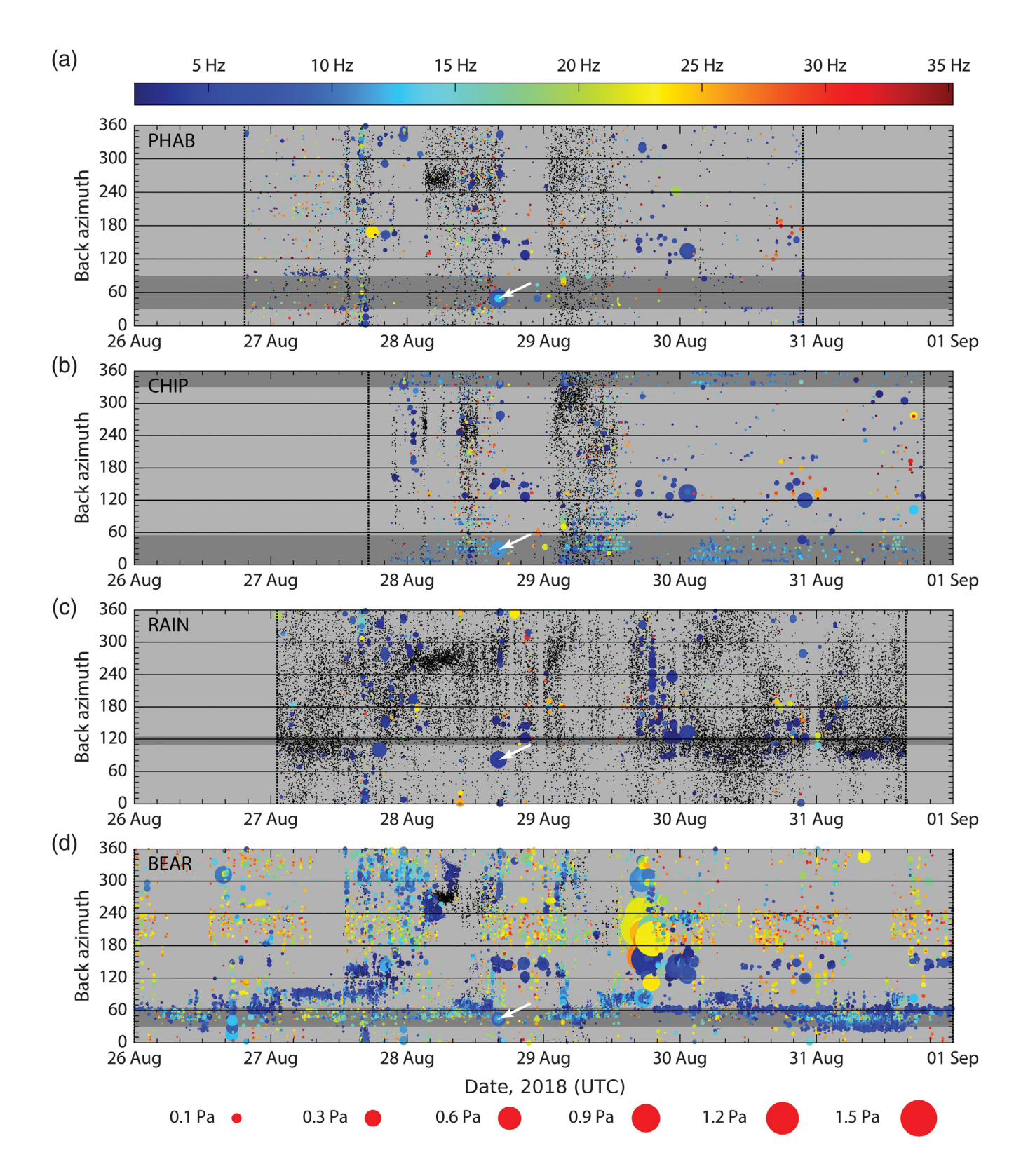


Figure 6. PMCC results from (a) PHAB, (b) CHIP, (c) RAIN, and (d) BEAR for 26–31 August 2018, showing highly variable detection sensitivity. Detections ≥2 Hz are scaled according to the maximum amplitude for each family and colored according to mean family frequency. Detections <2 Hz are shaded black and not scaled. Back azimuths are clockwise from north. Darker gray bars encompass the azimuth range of the upper basins of Cascade

Creek and Salt Creek for each station (Fig. 1a). Vertical dotted lines indicate the respective recording periods. At CHIP, a technical issue affected the data quality for the first 3.5 hr, resulting in a gap in the PMCC detections. All these detections are coherent infrasound arrivals, rather than noise, with the majority likely deriving from the numerous turbulent streams and waterfalls in the region. White arrows point to a glacial avalanche (Table 1).

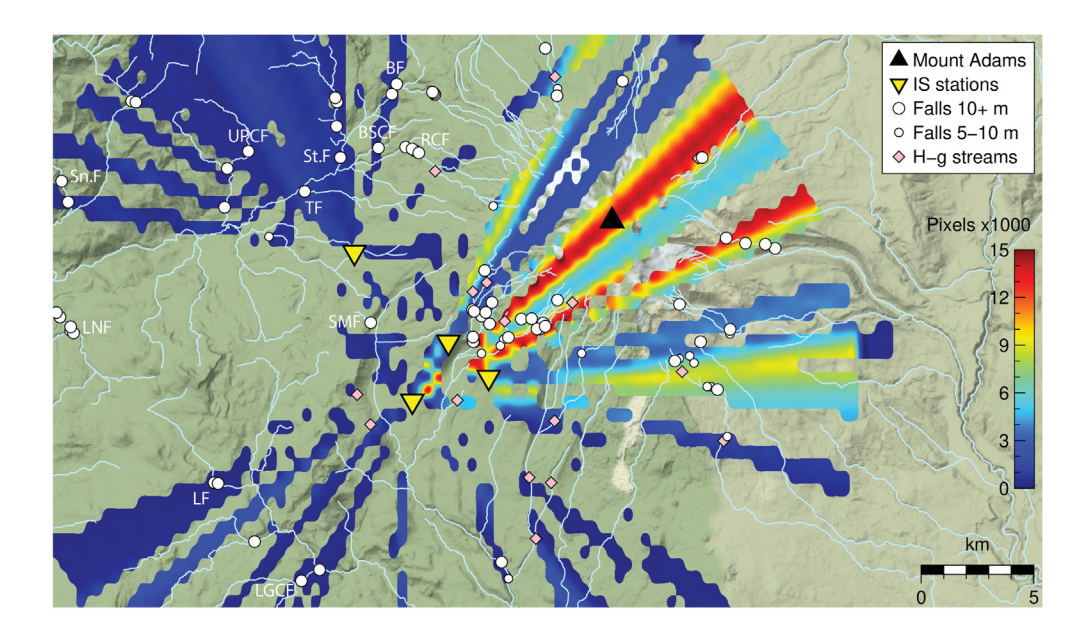


Figure 7. Back-azimuth intersections for 26–31 August 2018 Coordinated Universal Time (UTC) (grid-during layer from IMS-vASC) showing a high coincidence between infrasound arrival directions and turbulent waters. Total pixel counts (>275) are displayed for a grid square only if the nearest station detects a signal from the appropriate back azimuth, as well as any one other station. The positions of known waterfalls are indicated, along with selected high gradient (H-g) streams that align with IMS-vASC features. Some well-known waterfalls are labeled: BF, Babyshoe Falls; BSCF, Big Spring Creek Falls; LF, Langfield Falls; LGCF, Little Goose Creek Falls; LNF, Little Niagra Falls; RCF, Riley Creek Falls; SMF, Swampy Meadow Falls; Sn.F, Snagtooth Falls; St.F, Steamboat Falls; TF, Twin Falls; UPCF, Upper Pin Creek Falls.

particularly limited around RAIN, where several waterfalls are behind ridges or in deep canyons. More sources are detected when use of the closest station to the intersection is not required, but the configuration in Figure 7 more clearly outlines the effects of acoustic and topographic features. Drainages on Mount Adams coincide with the most dominant detections as anticipated. Falls with low discharge, such as Swampy Meadow Falls (~0.1 m³/s), may not be detected, despite being ~15 m in total height. Conversely, unidentified waterfalls may exist beneath the widespread dense tree coverage. Some intersection areas may be coincidental overlaps from temporally distinct events or derive from multiple arrays having similar back azimuths for the same event. An IMS-vASC video is provided in the supplemental material to illustrate the time evolution and episodic directionality of the detections.

In general, PHAB and CHIP had noticeably few detections, despite proximity to potential signal sources on Mount Adams (Fig. 7). We attribute this, in part, to their ridgetop locations, where widespread wildfires had led to sparse vegetation (Fig. 1) and relatively high wind noise (Hedlin *et al.*, 2002; Webster and Raspet, 2015). The wildfires meant that more forested sites in proximal areas were unavailable. Gaps in detections, as with BEAR, coincide with increases in wind noise (Fig. S3). Variation in proximity to sources, propagation conditions, and

station hardware noise floors may also be relevant. The station geometry is also likely to contribute to the detection discrepancy, because BEAR detections fall by ~50% when using only the outer three sensors. Global Positioning System (GPS) positional accuracy due to tree density (i.e., sensor location error of $\sim 2-3$ m) may also have affected array processing results. Because of the relatively poor detection rates for the temporary stations, we used lower signal association thresholds in PMCC.

Glacial avalanche. An avalanche occurred on the White Salmon Glacier on 28 August 2018 at ~16:01, as determined using infrasound and satellite imagery. Analyzing such events in detail helps constrain the detection, location, and modeling capabilities of the arrays. All four infrasound arrays clearly recorded the

event for 25 s, despite amplitudes below 0.3 Pa (Figs. 6 and 8a and Table 1). The mean frequency of PMCC families ranged from 4 Hz (RAIN) to 12 Hz (CHIP), with the full-frequency range between all sites 0.4-40 Hz. Such results depend on attenuation and SNR for each station. Waveforms begin emergently, are briefly dominated by two low-frequency (0.3-2.5 Hz) impulses, and then decay slowly. The event is preceded by 15 s by two broadband precursory signals (Fig. 8a) on all arrays except RAIN. The consistent time delay between precursory and main phases indicates a co-located source. Back azimuth and apparent velocity statistics for BEAR show sustained values during the precursory signals and main event (Fig. 8b). This consistency extends ~40 s earlier at BEAR, with additional impulsive signals detected (-32 to -18 s in Fig. 8b), though these features are not observed at the other arrays. Back-azimuth triangulation places the event at a steep (45°) bluff at the front of the upper White Salmon Glacier (Fig. 8c). Back azimuths are determined by averaging PMCC families with maximum frequencies up to 5 Hz. We find that incident angle estimates from each station do not converge on a specific elevation for a source, regardless of modeled mean path temperature or the family frequency range considered. RAIN tends to underestimate the angle, with BEAR overestimating (as is also the case for mass wasting events in Fig. 5). Without further calibration, the method has limited

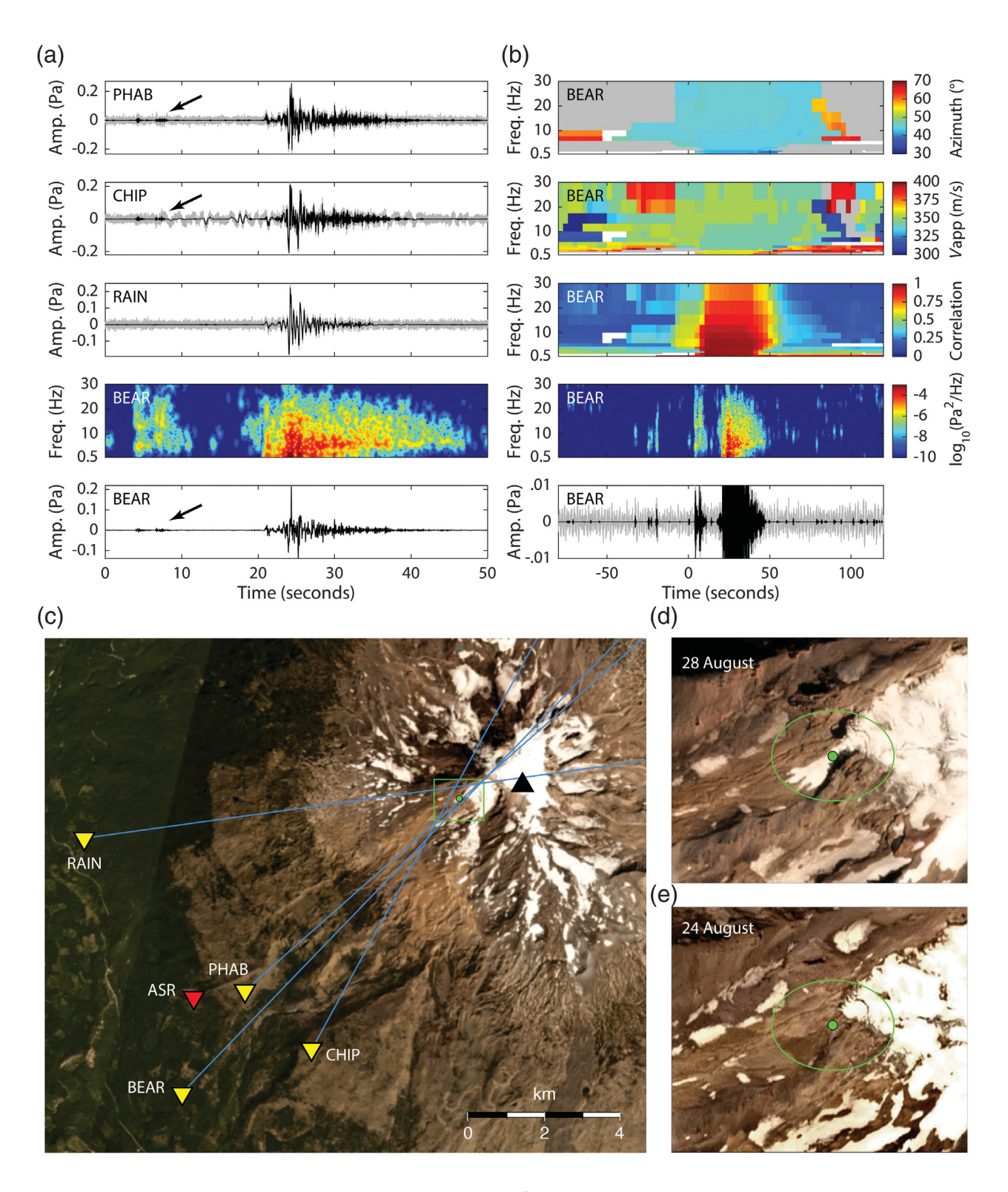


Figure 8. Glacial avalanche signal characteristics, array processing results, and derived location. (a) Beamformed infrasound waveforms from event on 28 August 2018 at \sim 16:01, for frequencies >0.5 Hz (gray) and subsequent denoising with a Wiener filter (black). Apparent velocities ($v_{\rm app}$) and back azimuths used in the beamforming are the means from PMCC families whose maximum frequency is 5 Hz. The spectrogram plots PSD at BEAR using the same scale as that in panel (b). Arrows point to weak precursory infrasound. (b) Expanded timeframe for same event from panel (a),

focusing on BEAR data. Back azimuth, $v_{\rm app}$, and correlation values derive from PMCC statistics. Gray pixels are off-scale; white means no pixels. Waveform clipping helps illustrate the precursory signals prior to 20 s. (c) Triangulation of PMCC back-azimuth values used in panel (a). The marked area around the intersection of back azimuths is expanded in panels (d,e), which also show the mean location provided by the inversion of sensor arrival times as a green dot, and the 95% confidence interval. The images in panels (c, d) are from 28 August 2018 at ~18:29.

application at BEAR, given that errors of a few degrees will give high-elevation uncertainties at remote source-station distances.

We also perform an iterative least-squares inversion of the 13 arrival times for the event using the location method of Geiger (1910, 1912), more recently addressed by, for example, Ge (2003), Stein and Wysession (2003), and Havskov and Ottemöller (2010). Altitude is allowed to vary in 10 m steps from 2500 to 3800 m, and velocity from 300 to 400 m/s in 2.5 m/s increments. One hundred inversions are performed, randomly perturbing the collective arrival times at each array by ±0.15 s, necessitating the adjustments of PHAB and CHIP be within 0.15 s of each other, given their similar locations. The resulting 95% confidence interval ellipsoid centers at the bluff within the triangulation mesh, spanning 540 m×400 m horizontally, 934 m vertically (Fig. 8d). The mean altitude is ~85 m above the corresponding elevation. Attempting to locate the event with just arrival times from BEAR provides a poor location estimate. Better results may be obtained using alternate location methods for single arrays, for example, Szuberla et al. (2006), Shani-Kadmiel et al. (2018), Green and Nippress (2019), and Shang et al. (2019).

Satellite photographs taken 2.5 hr after the located event show an ~20,000 m² area of glacial avalanche debris from the front of the upper White Salmon Glacier (Fig. 8d). Prior to the event, the closest images with clear views are four days prior, without evidence of debris (Fig. 8e). Ongoing instability is implied by rockfall debris in the same area at other times of year.

The infrasound signals themselves suggest a mixture of falling and flowing processes (Allstadt *et al.*, 2018, and references therein). The precursory components and emergent onset may reflect the initial detachment and failure stages (Zimmer *et al.*, 2012; Havens *et al.*, 2014; Schimmel *et al.*, 2017). Given the absence of real-time visual observations of the event, a detailed attribution of the infrasound source time function to a specific mass movement sequence is not possible. To a first order, however, we model the source time history as a hemispherical monopole in terms of the mass (M) of air displaced:

$$M(t) = 2\pi r \iint P(t) dt^2,$$

in which *P* is the pressure time series and *r* is the source-station distance (e.g., Lighthill, 2001; Oshima and Maekawa, 2001; Moran *et al.*, 2008). Figure 9 shows that the highest mass values are ~100 kg, equivalent to a sphere of ~6 m diameter (*d*), assuming an air density of 1 kg/m³. A monopole is applicable when the source is acoustically compact ($d \ll \lambda/2\pi$, λ is the wavelength) and recorded in the far field ($r \gg \lambda/2\pi$). Here, d = 6 m, $\lambda = 337.5$ m at 1 Hz, and r > 7700 m, thereby representing reasonable approximation by a monopole.

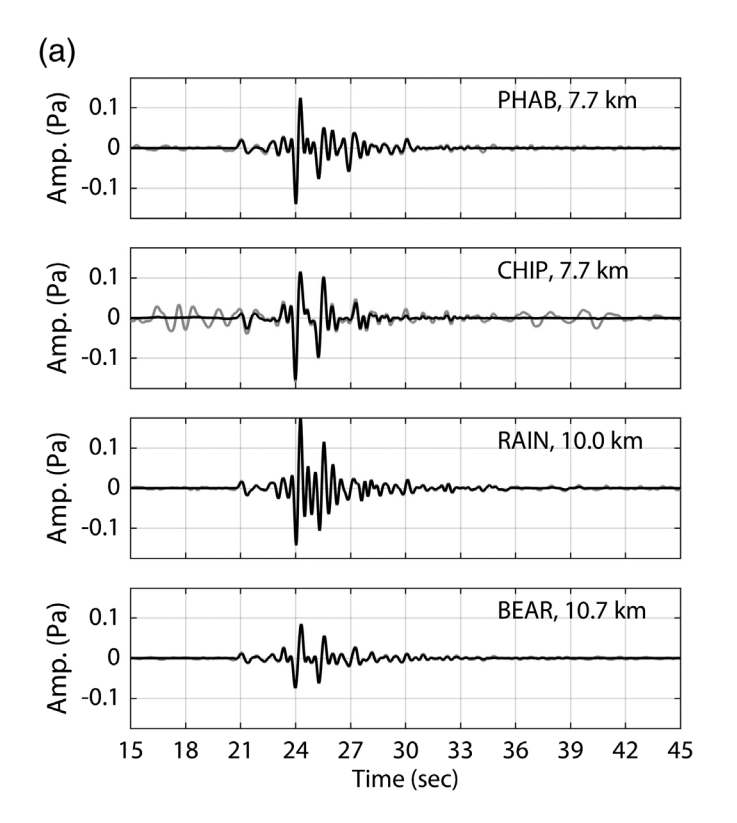
Multiple peaks during the source time function in Figure 9 may indicate repeat collapses from the glacier front. Given the size of the debris fan is much larger than that implied by the

mass values in the source time function, we speculate that contributing factors to the discrepancy may be (1) additional events occurred in the preceding four days that went undetected, (2) low turbulence of the flow front was inefficient in generating infrasound (e.g., Naugolnykh and Bedard, 2002; Mayer *et al.*, 2020), (3) little momentum was built up by the avalanche during the short (~300 m) unconstrained runout on a rough surface, with, for example, Kogelnig *et al.* (2011) showing a strong correlation between velocity and infrasound pressure for moving sources. Seismically, the event is barely above the background noise, due to an impaired sensor response.

Discussion

Our study is motivated by the potential of using infrasound to quickly detect, progressively locate, and swiftly alert people about oncoming large lahars, which are both hazardous and relatively infrequent at Mount Adams. To the extent that smaller mass movement events may be precursors or triggers to large events, we are initially aiming in this study to characterize sources of background noise, and identify thresholds and best methods for event detection using infrasound arrays. During our 3 yr study, several small debris flows or flow candidates were reported by local observers; however, we did not find signatures of these events in our data (Table 1). In contrast, we identified 12 events at BEAR that are possible candidates for mass movements based upon expected seismoacoustic signal characteristics. With one exception, none of these signals had local reports or other visual data to illuminate associated physical processes. Using additional temporary arrays, in addition to the main BEAR array, we were successful in locating and characterizing a glacial avalanche on the upper White Salmon Glacier. This event was confirmed using before and after satellite images. The corresponding local time for the event was early morning, with low wind typical of the time period improving potential SNR. In general, our results of mass movement observation are primarily limited by (1) infrequent events above the detection threshold of our arrays, (2) a lack of visual observations of activity for those candidate detections we do have, and (3) year-round background sound clutter from the direction of Mount Adams that is unrelated to mass wasting.

To quickly and accurately locate the incipient stages of hazardous lahars from the summit area of Mount Adams with infrasound, it may be beneficial to add permanent arrays nearer to source zones. The limited detection of known mass movements to date implies that improved SNR equipment design (e.g., Albert and Pankow, 2019, 2020) and preprocessing noise reduction strategies (e.g., Williams et al., 2020) would be of use for deployments in these more exposed areas, and where source amplitudes could be relatively low. Given permitting issues, however, potentially desirous solutions like low-cost and low-power telemetered systems that reduce preparation and installation time (e.g., Schimmel et al., 2018;



Ye et al., 2019), may prove challenging to implement. We find that when ASR is correctly operating, some small mass movement events are clearly detectable seismically (Fig. 5). Seismic propagation velocities mean that low alarm latency can be achieved at ASR, despite its location outside the wilderness boundary. A sole seismic station, however, has limited effectiveness in a monitoring capacity.

Notably, lahars can grow in volume as they propagate down drainages, which we have shown to be sources of (presumably) fluvial infrasound with many similar signal characteristics. Obvious changes in back azimuth with time can be indicative of flow fronts (e.g., Bosa et al., 2020), but static sound sources can develop during flows at waterfalls, check dams, and due to propagation effects caused by topography (e.g., Johnson and Palma, 2015; Marchetti et al., 2019). For a single array such as BEAR, these scenarios provide a strong challenge for automated signal detection, location, and modeling procedures. For one or more arrays, probabilistic analyses and modeling could potentially help establish confidence levels for detection thresholds for a range of network configurations (e.g., Le Pichon et al., 2009; Green and Bowers, 2010; Tailpied et al., 2013), given a priori assumed lahar source signal properties of amplitude, frequency content, duration, likely locations, and so forth (e.g., George and Iverson, 2014; Johnson and Palma, 2015; Allstadt et al., 2018; Watson et al., 2020). Such models should also account for (1) statistically characterized variations in site noise (wind noise) (e.g., Le Pichon et al., 2009; Green and Bowers, 2010; Brown et al., 2014), (2) local propagation (wind strength and direction, topography, temperature, and attenuation), and (3) variability in background clutter.

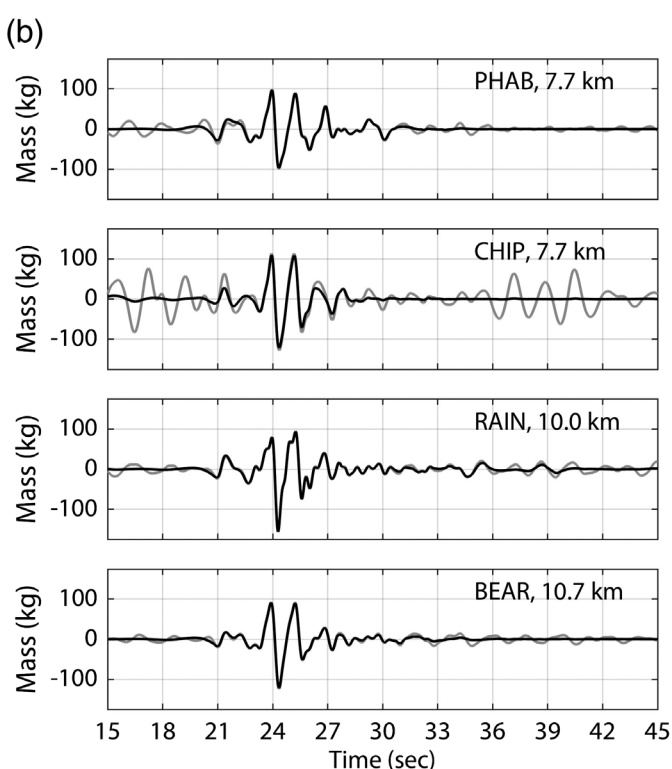


Figure 9. Glacial avalanche infrasound records and their equivalent mass source time functions. (a) Infrasound amplitudes at each array (0.5–3 Hz). Black traces have been denoised with a Wiener filter, gray traces have not. For CHIP, we remove remaining noise from 16 to 19 s by manually editing the spectral content with BCseis. The timescale matches that from Figure 8a. Distances are those between arrays and the mean source location provided by the travel-time inversion. (b) Mass equivalent source time functions for black and gray traces.

A more comprehensive monitoring strategy of Mount Adams could involve focused seismoacoustic and video surveillance of multiple key drainages (Fig. 1b) as well as weather sensors, flow gauges, and trip wires, in line with designs for areas of similar concern (e.g., Kogelnig *et al.*, 2014; Liu *et al.*, 2015; Chen *et al.*, 2016; Schimmel and Hübl, 2016; Moran, 2018; Marchetti *et al.*, 2019). Such diverse instrumentation would likely benefit detection sensitivity, flow-front location accuracy, avoiding false alarms, interpreting physical properties, and also tailoring any alerts to events of particular magnitude.

Conclusion

The BEAR infrasound array is the first at Mount Adams and lays groundwork for a system which could potentially detect and track lahars rumbling down the southwest flank. To date, BEAR, as well as three additional temporary arrays in August 2018, have helped meet initial goals by establishing ambient background wind-noise characteristics and likely sources of

clutter, as well as successfully locating a small glacial avalanche that was also visible in satellite imagery. This event was one of 12 suspected mass movements detected by BEAR during the study period. Other transient signals recorded include thunder and, possibly, icequakes. SNR, the primary factor controlling lahar detection, is presumably dictated mainly by source proximity, source size, and wind levels. Wind noise precluded detection of several witnessed small debris flows below the summit; however, it is more likely that large events of a hazardous nature would be detectable with the current instrumentation at BEAR and ASR. The drainages themselves appear to create abundant seasonal clutter from fluvial and waterfall infrasound, although, further confirmation of these sources (e.g., using flow-gauge or time-lapse video data) is needed. Characterizing this clutter is imperative for any future robust infrasonic lahar monitoring system, which should be supplemented by additional data types to reduce ambiguity. Novel real-time station designs may be required to meet environmental, budgetary, and logistical challenges in this remote region. Future work with more advanced processing methods may better characterize multiple clutter sources and wind noise, and could enhance signal detectability.

Data and Resources

Infrasound and seismic data are available from the Incorporated Research Institutions for Seismology (IRIS) Data Management Center (DMC) via links in the following citations: BEAR (UC Santa Barbara, 1989); PHAB, CHIP, and RAIN (Matoza and Haymon, 2018); ASR (University of Washington, 1963). Time-lapse camera images from BEAR documenting weather and equipment conditions are available at DOI: 10.25349/D9903G. Sensor specifications are published manufacturer values. Waterfall names and sizes derive from Northwest Waterfall Survey (https://www.waterfallsnorthwest.com) and Google Earth. BKRW1 wind and rainfall data are provided by MesoWest (https://mesowest.utah.edu), snow and temperature data by the National Oceanic and Atmospheric Administration (NOAA; https://www.ncdc.noaa.gov), river discharge data by the U.S. Geological Survey (USGS; https://waterdata.usgs.gov/nwis), and eventcoincident weather data by Ventusky (https://www.ventusky.com). Satellite images are via Planet Labs (https://www.planet.com). All websites were last accessed in August 2020. The supplemental material for this article includes extended information on detected events, system hardware, weather and hydrology data, as well as tools used for data processing, analysis, and plotting.

Declaration of Competing Interests

The authors acknowledge that there are no conflicts of interest recorded.

Acknowledgments

For their invaluable assistance, the authors wish to thank Seth Moran and Weston Thelen (Cascade Volcano Observatory, U.S. Geological Survey), Deborah Terrion, Erin Black, and Jon Nakae (U.S. Forest Service), Paul Hegarty, Chris Livsey, Sean Maher, and R. Pu (UC Santa Barbara), Howard Peavey (independent, technical advice),

and Jon Caryl (Mount Adams Tree Service). The authors are appreciative for support from the Lahar Event Awareness and Preparation group (LEAP), and the Friends of Mount Adams, especially Darryl Lloyd. The authors also thank Weston Thelen and two anonymous reviewers whose comments helped improve the article. This pilot project was funded by a UC Santa Barbara academic senate faculty research grant as well as student travel funds from the Department of Earth Science, UC Santa Barbara. Richard W. Sanderson and Robin S. Matoza were supported by National Science Foundation (NSF) Grants EAR–1614855 and EAR–1847736.

References

- Adam, V., V. Chritin, M. Rossi, and E. Lancker (1998). Infrasonic monitoring of snow-avalanche activity: What do we know and where do we go from here? *Ann. Glaciol.* **26**, 324–328, doi: 10.3189/1998AoG26-1-324-328.
- Albert, S., and K. L. Pankow (2019). Comparison of wind noise reduction systems for use in temporary infrasound deployments, *The AGU Fall Meeting*, San Francisco, California, Abstract S41E-0581.
- Albert, S., and K. L. Pankow (2020). Temporary wind noise reduction systems for infrasound: Comparison over time and response analysis, *The AGU Fall Meeting*, Abstract S006-01.
- Allstadt, K., and S. D. Malone (2014). Swarms of repeating stick-slip icequakes triggered by snow loading at Mount Rainier volcano, *J. Geophys. Res.* **119**, no. 5, 1180–1203, doi: 10.1002/2014JF003086.
- Allstadt, K. E., R. S. Matoza, A. B. Lockhart, S. C. Moran, J. Caplan-Auerbach, M. M. Haney, W. A. Thelen, and S. D. Malone (2018). Seismic and acoustic signatures of surficial mass movements at volcanoes, *J. Volcanol. Geoth. Res.* 364, 76–106, doi: 10.1016/j.jvolgeores.2018.09.007.
- Allstadt, K. E., B. G. McVey, and S. D. Malone (2017). Seismogenic landslides, debris flows, and outburst floods in the western United States and Canada from 1977 to 2017, *U.S. Geol. Surv. Data Release*, doi: 10.5066/F7251H3W.
- Anderson, J. F., T. J. Ronan, H. D. Ortiz, D. G. E. Gomes, J. R. Barber, J.
 B. Johnson, and J. P. McNamara (2019). Whitewater acoustics, *The AGU Fall Meeting*, San Francisco, California, Abstract H53O-2030.
- Arattano, M., and L. Marchi (2008). Systems and sensors for debrisflow monitoring and warning, *Sensors* **8**, no. 4, 2436–2452, doi: 10.3390/s8042436.
- Assink, J. D., L. G. Evers, I. Holleman, and H. Paulssen (2008). Characterization of infrasound from lightning, *Geophys. Res. Lett.* **35**, L15802, doi: 10.1029/2008GL034193.
- Bass, H. E. (1980). The propagation of thunder through the atmosphere, *J. Acoust. Soc. Am.* **67**, 1959–1966, doi: 10.1121/1.384354.
- Bosa, A., J. B. Johnson, S. De Angelis, J. J. Lyons, R. P. Escobar-Wolf, A. Roca, and A. Pineda (2020). Tracking secondary lahar flow paths and characterizing pulses and surges using infrasound array networks at Volcán Fuego, Guatemala, *The AGU Fall Meeting*, Abstract V009-03.
- Bowman, J. R., G. E. Baker, and M. Bahavar (2005). Ambient infrasound noise, *Geophys. Res. Lett.* **32,** L09803, doi: 10.1029/2005GL022486.
- Bowman, J. R., G. Shields, and M. S. O'Brien (2007). Infrasound station ambient noise estimates and models 2003–2006, *The 2007 Infrasound Technology Workshop*, Tokyo, Japan, 13–16 November, Abstract 5-5, available at https://l2a.ucsd.edu/local/

- Meetings/2007_ITW_Japan/Presentations/session_5/Bowman_infrasound_noise_Tokyo_ITW.ppt (last accessed August 2020).
- Brown, D., L. Ceranna, M. Prior, P. Mialle, and R. J. Le Bras (2014). The IDC seismic, hydroacoustic and infrasound global low and high noise models, *Pure Appl. Geophys.* **171**, 361–375, doi: 10.1007/s00024-012-0573-6.
- Burtin, A., L. Bollinger, J. Vergne, R. Cattin, and J. L. Nábělek (2008). Spectral analysis of seismic noise induced by rivers: A new tool to monitor spatiotemporal changes in stream hydrodynamics, *J. Geophys. Res.* 113, no. B05301, doi: 10.1029/2007JB005034.
- Campus, P., and D. R. Christie (2010). Worldwide observations of infrasonic waves, in *Infrasound Monitoring for Atmospheric Studies*, A. Le Pichon, E. Blanc, and A. Hauchecorne (Editors), Springer, Dordrecht, The Netherlands, 185–234, doi: 10.1007/978-1-4020-9508-5_6.
- Cansi, Y. (1995). An automatic seismic event processing for detection and location: The P.M.C.C. method, *Geophys. Res. Lett.* **22**, no. 9, 1021–1024, doi: 10.1029/95GL00468.
- Cansi, Y., and A. Le Pichon (2009). Infrasound event detection using the progressive multi-channel correlation algorithm, in *Handbook* of Signal Processing in Acoustics, D. Havelock, S. Kuwano, and M. Vorländer (Editors), Springer, New York, New York, 1425–1435, doi: 10.1007/978-0-387-30441-0_77.
- Chen, N.-S., J. I. Tanoli, G.-S. Hu, F.-N. Wang, C. L. Yang, H. T. Ding, N. He, and T. Wang (2016). Outlining a stepwise, multi-parameter debris flow monitoring and warning system: An example of application in Aizi Valley, China, J. Mt. Sci. 13, no. 9, 1527–1543, doi: 10.1007/s11629-015-3624-5.
- De Angelis, S., A. Diaz-Moreno, and L. Zuccarello (2019). Recent developments and applications of acoustic infrasound to monitor volcanic emissions, *Remote Sens.* **11**, no. 11, 1302, doi: 10.3390/rs11111302.
- de Groot-Hedlin, C. D., M. A. H. Hedlin, and K. T. Walker (2014). Detection of gravity waves across the USArray: A case study, *Earth Planet Sci. Lett.* **402**, 345–352, doi: 10.1016/j.epsl.2013.06.042.
- Díaz, J., M. Ruíz, L. Crescentini, A. Amoruso, and J. Gallart (2014). Seismic monitoring of an Alpine mountain river, J. Geophys. Res. 119, no. 4, 3276–3289, doi: 10.1002/2014JB010955.
- Farges, T., and E. Blanc (2010). Characteristics of infrasound from lightning and sprites near thunderstorm areas, *J. Geophys. Res.* **115,** A00E31, doi: 10.1029/2009JA014700.
- Fee, D., and M. Garcés (2007). Infrasonic tremor in the diffraction zone, *Geophys. Res. Lett.* **34**, L16826, doi: 10.1029/2007GL030616.
- Fee, D., and R. S. Matoza (2013). An overview of volcano infrasound: From Hawaiian to Plinian, local to global, *J. Volcanol. Geoth. Res.* **249**, 123–139, doi: 10.1016/j.jvolgeores.2012.09.002.
- Feng, H. N., Y. C. Yang, I. P. Chunchuzov, and P. X. Teng (2014). Study on infrasound from a water dam, *Acta Acustica United with Acustica* **100**, no. 2, 226–234, doi: 10.3813/AAA.918702.
- Finn, C. A., M. Desczcz-Pan, E. D. Anderson, and D. A. John (2007). Three-dimensional geophysical mapping of rock alteration and water content at Mount Adams, Washington: Implications for lahar hazards, *J. Geophys. Res.* **112**, no. B10204, doi: 10.1029/2006JB004783.
- Garcés, M., J. Aucan, D. Fee, P. Caron, M. Merrifield, R. Gibson, J. Bhattacharyya, and S. Shah (2006). Infrasound from large surf, Geophys. Res. Lett. 33, L05611, doi: 10.1029/2005GL025085.

- Garcés, M., A. Harris, C. Hetzer, J. Johnson, S. Rowland, E. Marchetti, and P. Okubo (2003). Infrasonic tremor observed at Kīlauea Volcano, Hawai'i, Geophys. Res. Lett. 30, no. 20, doi: 10.1029/2003GL018038.
- Garcés, M. A. (2013). On infrasound standards, part 1: Time, frequency, and energy scaling, *Inframatics* 2, no. 2, doi: 10.4236/inframatics.2013.22002.
- Ge, M. (2003). Analysis of source location algorithms—Part II: Iterative methods, *J. Acoust. Emission* **21,** 29–51, available at http://www.aewg.org/jae/JAE-Vol_21-2003.pdf (last accessed August 2020).
- Geiger, L. (1910). Herdbestimmung bei Erdbeben aus den Ankunftszeiten, Nachrichten der Königlichen Gesellschaft der Wissenschaften zu Göttingen, mathematisch-physikalische Klasse 4, 331–349 (in German).
- Geiger, L. (1912). Probability method for the determination of earth-quake epicenters from the arrival time only, *Bull. St. Louis Univ.* **8**, 60–71, available at http://digitalcollections.slu.edu/digital/collection/catalogs/id/6310/rec/118 (last accessed August 2020).
- George, D. L., and R. M. Iverson (2014). A depth-averaged debris-flow model that includes the effects of evolving dilatancy: 2. Numerical predictions and experimental tests, *Proc. Math. Phys. Eng. Sci.* 470, 20130820, doi: 10.1098/rspa.2013.0820.
- Green, D. N., and D. Bowers (2010). Estimating the detection capability of the International Monitoring System infrasound network, *J. Geophys. Res.* **115**, D18116, doi: 10.1029/2010JD014017.
- Green, D. N., R. S. Matoza, J. Vergoz, and A. Le Pichon (2012). Infrasonic propagation from the 2010 Eyjafjallajökull eruption: Investigating the influence of stratospheric solar tides, *J. Geophys. Res.* **117**, D21202, doi: 10.1029/2012JD017988.
- Green, D. N., and A. Nippress (2019). Infrasound signal duration: The effects of propagation distance and waveguide structure, *Geophys. J. Int.* **216**, no. 3, 1974–1988, doi: 10.1093/gji/ggy530.
- Griswold, J. P., T. C. Pierson, and J. A. Bard (2018). Modeled inundation limits of potential lahars from Mount Adams in the White Salmon River Valley, Washington, *U.S. Geol. Surv. Open-File Rept.* 2018-1013, doi: 10.3133/ofr20181013.
- Haney, M. M., A. R. Van Eaton, J. J. Lyons, R. L. Kramer, D. Fee, A. M. Iezzi, R. P. Ziak, J. Anderson, J. B. Johnson, J. L. Lapierre, *et al.* (2020). Characteristics of thunder and electromagnetic pulses from volcanic lightning at Bogoslof volcano, Alaska, *Bull. Volcanol.* 82, no. 15, 1–16, doi: 10.1007/s00445-019-1349-y.
- Havens, S., H.-P. Marshall, J. B. Johnson, and B. Nicholson (2014). Calculating the velocity of a fast-moving snow avalanche using an infrasound array, *Geophys. Res. Lett.* 41, 6191–6198, doi: 10.1002/ 2014GL061254.
- Havskov, J., and L. Ottemöller (2010). Routine Data Processing in Earthquake Seismology: With Sample Data, Exercises and Software, Springer, Dordrecht, The Netherlands, doi: 10.1007/978-90-481-8697-6.
- Hedlin, M. A. H., J. Berger, and F. L. Vernon (2002). Surveying infrasonic noise on oceanic islands, *Pure Appl. Geophys.* **159**, 1127–1152, doi: 10.1007/s00024-002-8675-1.
- Hildreth, W., and J. Fierstein (1995). Geologic map of the Mount Adams volcanic field, Cascade Range of southern Washington, U.S. Geol. Surv. Map I-2460, scale 1:50,000, doi: 10.3133/i2460.
- Hsu, L., N. J. Finnegan, and E. E. Brodsky (2011). A seismic signature of river bedload transport during storm events, *Geophys. Res. Lett.* **38**, no. 13, doi: 10.1029/2011GL047759.

- Huang, C.-J., C.-H. Yeh, C.-Y. Chen, and S.-T. Chang (2008). Ground vibrations and airborne sounds generated by motion of rock in a river bed, *Nat. Hazards Earth Syst. Sci.* **8,** no. 5, 1139–1147, doi: 10.5194/nhess-8-1139-2008.
- Hürlimann, M., V. Coviello, C. Bel, X. Guo, M. Berti, C. Graf, J. Hübl, S. Miyata, J. B. Smith, and H.-Y. Yin (2019). Debris-flow monitoring and warning: Review and examples, *Earth Sci. Rev.* 199, doi: 10.1016/j.earscirev.2019.102981.
- Johnson, J. B., J. Anderson, S. De Angelis, R. P. Escobar-Wolf, J. J. Lyons, H.-P. Marshall, and A. Pineda (2019). On the capabilities of networked infrasound arrays for investigating rapid gravity-driven mass movements: Lahars and snow avalanches, *The AGU Fall Meeting*, San Francisco, California, Abstract V44B-02.
- Johnson, J. B., R. O. Arechiga, R. J. Thomas, H. E. Edens, J. Anderson, and R. Johnson (2011). Imaging thunder, *Geophys. Res. Lett.* 38, L19807, doi: 10.1029/2011GL049162.
- Johnson, J. B., J. M. Lees, and H. Yepes (2006). Volcanic eruptions, lightning, and a waterfall: Differentiating the menagerie of infrasound in the Ecuadorian jungle, *Geophys. Res. Lett.* 33, L06308, doi: 10.1029/2005GL025515.
- Johnson, J. B., and J. Palma (2015). Lahar infrasound associated with Volcan Villarrica's 3 March 2015 eruption, *Geophys. Res. Lett.* 42, no. 15, 6324–6331, doi: 10.1002/2015GL065024.
- Johnson, J. B., and T. J. Ronan (2015). Infrasound from volcanic rockfalls, J. Geophys. Res. Solid Earth 120, 8223–8239, doi: 10.1002/ 2015JB012436.
- Kim, K., A. Rodgers, and D. Seastrand (2018). Local infrasound variability related to in situ atmospheric observation, *Geophys. Res. Lett.* **45**, 2954–2962, doi: 10.1002/2018GL077124.
- Kogelnig, A., J. Hübl, E. Suriñach, I. Vilajosana, and B. W. McArdell (2014). Infrasound produced by debris flow: Propagation and frequency content evolution, *Nat. Hazards* 70, 1713–1733, doi: 10.1007/s11069-011-9741-8.
- Kogelnig, A., E. Suriñach, I. Vilajosana, J. Hübl, B. Sovilla, M. Hiller, and F. Dufour (2011). On the complementariness of infrasound and seismic sensors for monitoring snow avalanches, *Nat. Hazards Earth Syst. Sci.* 11, 2355–2370, doi: 10.5194/nhess-11-2355-2011.
- Langston, C. A., and S. M. Mousavi (2018). Adaptive seismic denoising based on the synchrosqueezed-continuous wavelet transform and block-thresholding, *Final Technical Rept. AFRL-RV-PS-TR-2018-0074*, Air Force Research Laboratory, https://apps.dtic.mil/sti/pdfs/AD1061053.pdf (last accessed August 2020).
- Leng, X.-P., D.-L. Liu, F.-Q. Wei, Y. Hong, and D.-F. Dai (2017). Debris flows monitoring and localization using infrasonic signals, *J. Mt. Sci.* **14**, 7, doi: 10.1007/s11629-016-3836-3.
- Le Pichon, A., R. Matoza, N. Brachet, and Y. Cansi (2010). Recent enhancements of the PMCC infrasound signal detector, *Inframatics* **26**, 5–8.
- Le Pichon, A., J. Vergoz, E. Blanc, J. Guilbert, L. Ceranna, L. Evers, and N. Brachet (2009). Assessing the performance of the International Monitoring System's infrasound network: Geographical coverage and temporal variabilities, *J. Geophys. Res. Atmos.* 114, D08112, doi: 10.1029/2008JD010907.
- Lighthill, J. (2001). Waves in Fluids, Second Ed., Cambridge University Press, Cambridge, United Kingdom, 524 p.
- Liu, D., D. Tang, S. Zhang, X. Leng, K. Hu, and L. He (2020). Method for feature analysis and intelligent recognition of infrasound

- signals of soil landslides, *Bull. Eng. Geol. Environ.* **43**, doi: 10.1007/s10064-020-01982-w.
- Liu, D. L., X. P. Leng, F. Q. Wei, S. J. Zhang, and Y. Hong (2015). Monitoring and recognition of debris flow infrasonic signals, J. Mt. Sci. 12, no. 4, 797–815, doi: 10.1007/s11629-015-3471-4.
- Lloyd, D. (2018). Ever Wild: A Lifetime on Mount Adams, RLO Media Productions, Portland, Oregon, 160 p.
- Lombardi, D., I. Gorodetskaya, G. Barruol, and T. Camelbeeck (2019). Thermally induced icequakes detected on blue ice areas of the East Antarctic ice sheet, *Ann. Glaciol.* **60**, no. 79, 45–56, doi: 10.1017/aog.2019.26.
- Maher, R. C., and S. R. Shaw (2008). Deciphering gunshot recordings, Proc. 33rd International Conf. Audio Engineering Society: Audio Forensics—Theory and Practice, Paper Number 2, Denver, CO, June.
- Major, J. J., T. C. Pierson, and J. W. Vallance (2018). Lahar—River of volcanic mud and debris, U.S. Geol. Surv. Fact Sheet 2018-3024, doi: 10.3133/fs20183024.
- Marchetti, E., M. Ripepe, G. Ulivieri, and A. Kogelnig (2015). Infrasound array criteria for automatic detection and front velocity estimation of snow avalanches: Towards a real-time early-warning system, *Nat. Hazards Earth Syst. Sci.* **15**, no. 11, 2545–2555, doi: 10.5194/nhess-15-2545-2015.
- Marchetti, E., F. Walter, G. Barfucci, R. Genco, M. Wenner, M. Ripepe, B. McArdell, and C. Price (2019). Infrasound array analysis of debris flow activity and implication for early warning, *J. Geophys. Res.* **124,** no. 2, 567–587, doi: 10.1029/2018JF004785.
- Marty, J. (2019). The IMS infrasound network: Current status and technological developments, in *Infrasound Monitoring for Atmospheric Studies: Challenges in Middle-Atmosphere Dynamics and Societal Benefits*, A. Le Pichon, E. Blanc, and A. Hauchecorne (Editors), Springer, Cham, Switzerland, 3–62, doi: 10.1007/978-3-319-75140-5_1.
- Matoza, R., D. Fee, D. Green, and P. Mialle (2019). Volcano infrasound and the International Monitoring System, in *Infrasound Monitoring* for Atmospheric Studies: Challenges in Middle-Atmosphere Dynamics and Societal Benefits, A. Le Pichon, E. Blanc, and A. Hauchecorne (Editors), Springer, Cham, Switzerland, 1023–1077, doi: 10.1007/978-3-319-75140-5_33.
- Matoza, R. S., M. A. Garcés, B. A. Chouet, L. D'Auria, M. A. H. Hedlin, C. De Groot-Hedlin, and G. P. Waite (2009). The source of infrasound associated with long-period events at Mount St. Helens, *J. Geophys. Res.* 114, no. B04305, doi: 10.1029/2008JB006128.
- Matoza, R. S., D. N. Green, A. Le Pichon, P. M. Shearer, D. Fee, P. Mialle, and L. Ceranna (2017). Automated detection and cataloging of global explosive volcanism using the International Monitoring System infrasound network, *J. Geophys. Res.* 122, 2946–2971, doi: 10.1002/2016/B013356.
- Matoza, R. S., and R. M. Haymon (2018). *Mount Adams Temporary Infrasound Arrays [Data set]*, International Federation of Digital Seismograph Networks, doi: 10.7914/SN/8J_2018.
- Matoza, R. S., M. A. H. Hedlin, and M. A. Garces (2007). An infrasound array study of Mount St. Helens, *J. Volcanol. Geoth. Res.* **160**, 249–262, doi: 10.1016/j.jvolgeores.2006.10.006.
- Matoza, R. S., M. Landès, A. Le Pichon, L. Ceranna, and D. Brown (2013). Coherent ambient infrasound recorded by the International Monitoring System, *Geophys. Res Lett.* 40, 429–433, doi: 10.1029/2012GL054329.

- Matoza, R. S., J. Vergoz, A. Le Pichon, L. Ceranna, D. N. Green, L. G.
 Evers, M. Ripepe, P. Campus, L. Liszka, T. Kvaerna, *et al.* (2011).
 Long-range acoustic observations of the Eyjafjallajökull eruption,
 Iceland, April–May 2010, *Geophys. Res. Lett.* 38, L06308, doi: 10.1029/2011GL047019.
- Mayer, S., A. van Herwijnen, G. Ulivieri, and J. Schweizer (2020). Evaluating the performance of an operational infrasound avalanche detection system at three locations in the Swiss Alps during two winter seasons, *Cold Regions Sci. Tech.* **173**, doi: 10.1016/j.coldregions.2019.102962.
- McNamara, D. E., and R. P. Buland (2004). Ambient noise levels in the continental United States, *Bull. Seismol. Soc. Am.* **94**, no. 4, 1517–1527, doi: 10.1785/012003001.
- Mills, H. H. (1991). Temporal variation of mass-wasting activity in Mount St. Helens crater, Washington, U.S.A., indicated by seismic activity, Arct. Antarct. Alp. Res. 23, 417–423, doi: 10.2307/1551683.
- Moore, J. R., K. L. Pankow, S. R. Ford, K. D. Koper, J. M. Hale, J. Aaron, and C. F. Larsen (2017). Dynamics of the Bingham Canyon rock avalanches (Utah, USA) resolved from topographic, seismic, and infrasound data, *J. Geophys. Res.* 122, 615–640, doi: 10.1002/2016JF004036.
- Moran, S. C. (2005). Seismic monitoring at Cascade volcanic centers, 2004—Status and recommendations, *U.S. Geol. Surv. Sci. Investig. Rept.* 2004-5211, 28 pp., available at https://pubs.usgs.gov/sir/2004/5211/ (last accessed August 2020).
- Moran, S. C. (2018). Mitigating volcanic hazards through geophysical monitoring and research, *The 2018 Workshop*, IRIS, Albuquerque, New Mexico, Abstract 4-3.
- Moran, S. C., R. S. Matoza, M. A. Garcés, M. A. H. Hedlin, D. Bowers, W. E. Scott, D. R. Sherrod, and J. W. Valance (2008). Seismic and acoustic recordings of an unusually large rockfall at Mount St. Helens, Washington, *Geophys. Res Lett.* 35, L10302, doi: 10.1029/2008GL035176.
- Naugolnykh, K., and A. Bedard (2002). A model of the avalanche infrasound radiation, Proc. 2002 IEEE International Geoscience and Remote Sensing Symposium/24th Canadian Symposium Remote Sensing, 871–872, doi: 10.1109/IGARSS.2002.1025713.
- Norris, R. D. (1994). Seismicity of rockfalls and avalanches at three Cascade Range volcanoes: Implications for seismic detection of hazardous mass movements, *Bull. Seismol. Soc. Am.* **84**, no. 6, 1925–1939.
- Oshima, H., and T. Maekawa (2001). Excitation process of infrasonic waves associated with Merapi-type pyroclastic flow as revealed by a new recording system, *Geophys. Res. Lett.* **28**, no. 6, 1099–1102, doi: 10.1029/1999GL010954.
- Pierson, T. C., R. J. Janda, J.-C. Thouret, and C. A. Borrero (1990).
 Perturbation and melting of snow and ice by the 13 November eruption of Nevado del Ruiz, Colombia, and consequent mobilization, flow and deposition of lahars, *J. Volcanol. Geoth. Res.* 41, nos. 1/4, 17–66, doi: 10.1016/0377-0273(90)90082-Q.
- Pierson, T. C., N. J. Wood, and C. L. Driedger (2014). Reducing risk from lahar hazards: Concepts, case studies, and roles for scientists, *J. Appl. Volcanol.* **3**, no. 16, 1–25, doi: 10.1186/s13617-014-0016-4.
- Pilger, C., L. Ceranna, J. O. Ross, J. Vergoz, A. Le Pichon, N. Brachet, E. Blanc, J. Kero, L. Liszka, S. Gibbons, et al. (2018). The European Infrasound Bulletin, Pure Appl. Geophys. 175, 3619–3638, doi: 10.1007/s00024-018-1900-3.

- Plapous, C., C. Marro, and P. Scalart (2006). Improved signal-to-noise ratio estimation for speech enhancement, *IEEE Trans. Audio Speech Lang. Process.* **14,** no. 6, 2098–2108, doi: 10.1109/TASL .2006.872621.
- Raspet, R., J.-P. Abbott, J. Webster, J. Yu, C. Talmadge, K. Alberts II, S. Collier, and J. Noble (2019). New systems for wind noise reduction for infrasonic measurements, in *Infrasound Monitoring for Atmospheric Studies: Challenges in Middle-Atmosphere Dynamics and Societal Benefits*, A. Le Pichon, E. Blanc, and A. Hauchecorne (Editors), Springer, Cham, Switzerland, 91–124, doi: 10.1007/978-3-319-75140-5_3.
- Richardson, J. P., G. P. Waite, W. D. Pennington, R. M. Turpening, and J. M. Robinson (2012). Icequake locations and discrimination of source and path effects with small aperture arrays, Bering Glacier terminus, AK, J. Geophys. Res. 117, F04013, doi: 10.1029/2012JF002405.
- Ronan, T. J., J. M. Lees, T. D. Mikesell, J. F. Anderson, and J. B. Johnson (2017). Acoustic and seismic fields of hydraulic jumps at varying Froude numbers, *Geophys. Res. Lett.* 44, 9734–9741, doi: 10.1002/2017GL074511.
- Roth, D. L., E. E. Brodsky, N. J. Finnegan, D. Rickenmann, J. M. Turowski, and A. Badoux (2016). Bed load sediment transport inferred from seismic signals near a river, J. Geophys. Res. 121, no. 4, 725–747, doi: 10.1002/2015JF003782.
- Schimmel, A., and J. Hübl (2016). Automatic detection of debris flows and debris floods based on a combination of infrasound and seismic signals, *Landslides* **13**, 1181–1196, doi: 10.1007/s10346-015-0640-z.
- Schimmel, A., J. Hübl, R. Koschuch, and I. Reiweger (2017). Automatic detection of avalanches: evaluation of three different approaches, *Nat. Hazards* 87, 83–102, doi: 10.1007/s11069-017-2754-1.
- Schimmel, A., J. Hübl, B. W. McArdell, and F. Walter (2018). Automatic identification of Alpine mass movements by a combination of seismic and infrasound sensors, *Sensors* 18, no. 5, 1658, doi: 10.3390/s18051658.
- Schmandt, B., R. C. Aster, D. Scherler, V. C. Tsai, and K. Karlstrom (2013). Multiple fluvial processes detected by riverside seismic and infrasound monitoring of a controlled flood in the Grand Canyon, *Geophys. Res. Lett.* 40, no. 18, 4858–4863, doi: 10.1002/grl.50953.
- Scott, W. E. (2010). Mount Adams—Summary of current volcanic, hydrologic, and hazard issues, *The 2010 Klickitat-White Salmon Science Conf.*, The Dalles, Oregon, Abstract 03, available at http://www.ykfp.org/klickitat/SciCon/SciCon10/SciCon10_pdf/03_WScott_KWS_WEB.pdf (last accessed August 2020).
- Scott, W. E., R. M. Iverson, J. W. Vallance, and W. Hildreth (1995). Volcano hazards in the Mount Adams region, Washington, U.S. Geol. Surv. Open-File Rept. 95-492, doi: 10.3133/ofr95492.
- Shang, C., P. Teng, J. Lyu, J. Yang, and H. Sun (2019). Infrasonic source altitude localization based on an infrasound ray tracing propagation model, J. Acoust. Soc. Am. 145, no. 6, 3805–3816, doi: 10.1121/1.5110712.
- Shani-Kadmiel, S., J. D. Assink, P. S. M. Smets, and L. G. Evers (2018). Seismoacoustic coupled signals from earthquakes in central Italy: Epicentral and secondary sources of infrasound, *Geophys. Res. Lett* 45, no. 1, 427–435, doi: 10.1002/2017GL076125.
- Stähli, M., M. Sättele, C. Huggel, B. W. McArdell, P. Lehmann, A. Van Herwijnen, A. Berne, M. Schleiss, A. Ferrari, A. Kos, *et al.* (2015).

- Monitoring and prediction in early warning systems for rapid mass movements, *Nat. Hazards Earth Syst. Sci.* **15,** 905–917, doi: 10.5194/nhess-15-905-2015.
- Stein, S., and M. Wysession (2003). *Introduction to Seismology, Earthquakes and Earth Structure*, Blackwell, Oxford, United Kingdom, 498 p.
- Szuberla, C. A. L., K. M. Arnoult, and J. V. Olson (2006). Discrimination of near-field infrasound sources based on timedifference of arrival information, *J. Acoust. Soc. Am.* 120, no. 3, EL23–EL28, doi: 10.1121/1.2234517.
- Tailpied, D., A. Le Pichon, E. Marchetti, M. Ripepe, M. Kallel, L. Ceranna, and N. Brachet (2013). Remote infrasound monitoring of Mount Etna: Observed and predicted network detection capability, *Inframatics* 2, no. 1, 1–11, doi: 10.4236/inframatics .2013.21001.
- Thüring, T., M. Schoch, A. van Herwijnen, and J. Schweizer (2015). Robust snow avalanche detection using supervised machine learning with infrasonic sensor arrays, *Cold Regions Sci. Tech.* **111**, 60–66, doi: 10.1016/j.coldregions.2014.12.014.
- Tsai, V. C., B. Minchew, M. P. Lamb, and J.-P. Ampuero (2012). A physical model for seismic noise generation from sediment transport in rivers, *Geophys. Res. Lett.* 39, no. 2, doi: 10.1029/2011GL050255.
- UC Santa Barbara (1989). UC Santa Barbara Engineering Seismology Network [Data set], International Federation of Digital Seismograph Networks, doi: 10.7914/SN/SB.
- Ulivieri, G., E. Marchetti, M. Ripepe, I. Chiambretti, G. De Rosa, and V. Segor (2011). Monitoring snow avalanches in northwestern Italian Alps using an infrasound array, *Cold Regions Sci. Tech.* **69**, nos. 2/3, 177–183, doi: 10.1016/j.coldregions.2011.09 .006.
- University Of Washington (1963). *Pacific Northwest Seismic Network* [Data set], International Federation of Digital Seismograph Networks, doi: 10.7914/SN/UW.
- Vallance, J. W. (1999). Postglacial lahars and potential hazards in the White Salmon River system on the southwest flank of Mount Adams, Washington, U.S. Geol. Surv. 2161, doi: 10.3133/b2161.
- Walsh, B., V. Coviello, L. Capra, J. Procter, and V. Márquez-Ramirez (2020). Insights into the internal dynamics of natural lahars from analysis of 3-component broadband seismic signals at Volcán de Colima, Mexico, *Front. Earth Sci.* 8, 542,116, doi: 10.3389/ feart.2020.542116.

- Watson, L. M., J. Dufek, E. M. Dunham, and D. Mohhaddes (2020). Computational aeroacoustic simulations of infrasound signals from volcanic eruptions, *The AGU Fall Meeting*, Abstract S006-06.
- Webster, J., and R. Raspet (2015). Infrasonic wind noise under a deciduous tree canopy, *J. Acoust. Soc. Am.* **137**, no. 5, 2670–2677, doi: 10.1121/1.4919340.
- Wenner, M., F. Walter, M. J. Chmiel, Z. Zhang, and B. W. McArdell (2020). Comprehensive exploitation of seismic data at a debris flow torrent—Early warning, hazard assessment, parameter estimation, *The AGU Fall Meeting*, Abstract S025-03.
- Williams, R. A., A. Perttu, and B. Taisne (2020). Processing of volcano infrasound using film sound audio post-production techniques to improve signal detection via array processing, *Geosci. Lett.* 7, no. 9, 1–13, doi: 10.1186/s40562-020-00158-4.
- Wilson, D. K., C. L. Pettit, and V. E. Ostashev (2015). Sound propagation in the atmospheric boundary layer, *Acoust. Today* 11, no. 2, 44–52, available at https://acousticstoday.org/sound-propagation-in-the-atmospheric-boundary-layer-d-keith-wilson-chris-l-pettit-and-vladimir-e-ostashev/ (last accessed August 2020).
- Woodward, R., H. Israelsson, I. Bondár, K. McLaughlin, J. R. Bowman, and H. Bass (2005). Understanding wind-generated infrasound noise, Proc. 27th Seismic Research Review: Ground-Based Nuclear Explosion Monitoring Technologies, 866–875, available at https:// www.osti.gov/servlets/purl/1027447 (last accessed August 2020).
- Ye, J., Y. Kurashima, T. Kobayashi, H. Tsuda, T. Takahara, and W. Sakurai (2019). An efficient in-situ debris flow monitoring system over a wireless accelerometer network, *Remote Sens.* 11, no. 13, 1512, doi: 10.3390/rs11131512.
- Yount, J., A. Naisbitt, and E. D. Scott (2008). Operational highway avalanche forecasting using the infrasonic avalanche detection system, *Proc. 2008 International Snow Science Workshop*, 265–276, https://arc.lib.montana.edu/snow-science/objects/P__8187.pdf (last accessed August 2020).
- Zimmer, V. L., B. D. Collins, G. M. Stock, and N. Sitar (2012). Rock fall dynamics and deposition: An integrated analysis of the 2009 Ahwiyah Point rock fall, Yosemite National Park, USA, *Earth Surf. Process. Landf.* 37, 680–691, doi: 10.1002/esp.3206.

Manuscript received 2 October 2020 Published online 12 May 2021